National Renewable Energy Laboratory
A national laboratory of the U.S. Department of Energy
Office of Energy Efficiency & Renewable Energy
Innovation for Our Energy Future

Novel Materials Development for Polycrystalline Thin-Film Solar Cells

Final Subcontract Report
26 July 2004 – 15 June 2008

D.A. Keszler and J.F. Wager
Oregon State University
Corvallis, Oregon

Subcontract Report
NREL/SR-520-44020
November 2008

NREL is operated for DOE by the Alliance for Sustainable Energy, LLC Contract No. DE-AC36-08-GO28308

Novel Materials Development for Polycrystalline Thin-Film Solar Cells

Subcontract Report
NREL/SR-520-44020
November 2008

Final Subcontract Report
26 July 2004 – 15 June 2008

D.A. Keszler and J.F. Wager
Oregon State University
Corvallis, Oregon

NREL Technical Monitor: Fannie Posey Eddy

Prepared under Subcontract No. XAT-4-33624-11

National Renewable Energy Laboratory
1617 Cole Boulevard, Golden, Colorado 80401-3393
303-275-3000 • www.nrel.gov

NREL is a national laboratory of the U.S. Department of Energy
Office of Energy Efficiency and Renewable Energy
Operated by the Alliance for Sustainable Energy, LLC

Contract No. DE-AC36-08-GO28308

This publication was reproduced from the best available copy submitted by the subcontractor and received no editorial review at NREL

NOTICE

This report was prepared as an account of work sponsored by an agency of the United States government. Neither the United States government nor any agency thereof, nor any of their employees, makes any warranty, express or implied, or assumes any legal liability or responsibility for the accuracy, completeness, or usefulness of any information, apparatus, product, or process disclosed, or represents that its use would not infringe privately owned rights. Reference herein to any specific commercial product, process, or service by trade name, trademark, manufacturer, or otherwise does not necessarily constitute or imply its endorsement, recommendation, or favoring by the United States government or any agency thereof. The views and opinions of authors expressed herein do not necessarily state or reflect those of the United States government or any agency thereof.

Available electronically at http://www.osti.gov/bridge

Available for a processing fee to U.S. Department of Energy and its contractors, in paper, from:

U.S. Department of Energy
Office of Scientific and Technical Information
P.O. Box 62
Oak Ridge, TN 37831-0062
phone: 865.576.8401
fax: 865.576.5728
email: mailto:reports@adonis.osti.gov

Available for sale to the public, in paper, from:

U.S. Department of Commerce
National Technical Information Service
5285 Port Royal Road
Springfield, VA 22161
phone: 800.553.6847
fax: 703.605.6900
email: orders@ntis.fedworld.gov
online ordering: http://www.ntis.gov/ordering.htm

Printed on paper containing at least 50% wastepaper, including 20% postconsumer waste

Table of Contents

Abstract iv

1. Introduction 1

2. Schottky Barrier Theory 2

3. Heterojunction Theory 4

4. p-Layer Insertion 6
   4.1 Materials Parameters 6
   4.2 Schottky Barrier Assessment 8
   4.3 Heteojunctions 11
   4.4 SCTF Ionization Potential Reassessment 14

5. Conclusions 15

References 16

Abstract

The simplest realization of a pin double-heterojunction thin-film solar cell would consist of a lightly-doped, moderate-bandgap absorber i-layer; a heavily-doped, wide-bandgap n-layer window (cathode); and a heavily-doped, wide-bandgap p-layer window (anode) in which the anode and cathode are electrically contacted by at least one transparent conductor. The focus herein is on p-layer interfacial assessment, which is accomplished using modern Schottky barrier and heterojunction theory and is directed to the analysis of p-windows for copper indium gallium diselenide (CIGS) and cadmium telluride (CdTe) thin-film solar cells. A p-type window layer serves as an electron reflector and also aids in the formation of an ohmic anode contact. Ohmic anode contacts are particularly difficult to form in CIGS and CdTe thin-film solar cells since these materials have very large ionization potentials, i.e., IP_S = 5.65 (CIGS) and 5.78 V (CdTe) and significant interfacial screening, characterized by extremely small Schottky barrier interface parameters, i.e., S = 0.14 (CIGS) and 0.21 (CdTe). An ideal p-type window material would be heavily-doped, p-type, and would have a wide bandgap, a large ionization potential, and a smaller charge neutrality level energy than that of the absorber layer.

1 Introduction

Figure 1 illustrates an idealized energy band diagram for a pin double-hetero-junction thin-film solar cell which is of primary interest to the work discussed herein. This device possesses three layers, an n-type window, an absorber, and a p-type window. Typically, the absorber is lightly p-doped, since in most semiconductors photovoltaic carrier separation and transport is more efficient when accomplished using photo-generated minority carrier electrons. The bandgaps of the n- and p-type windows are indicated in Fig. 1 as being significantly wider than that of the absorber, since these bandgap differences give rise to interfacial valence and conduction band discontinuities, respectively, and concomitant hole and electron reflecting barriers. Such barriers are useful for suppressing undesirable carrier recombination at anode and cathode contacts. Additionally, it is beneficial for n- and p-type window layers to have wide bandgaps so that they are transparent to the relevant portion of the electromagnetic spectrum to be harvested by the absorber layer. Having a wide bandgap window layer is especially attractive in tandem or multi-junction solar cells. Typically, these n- and p-type windows are heavily doped, with the intent of facilitating the formation of ohmic contacts between the absorber and the cathode and anode contact. If a window layer possesses a sufficiently high doping density, it together with its metal or transparent conducting contact can function as a tunneling ohmic interface, irrespective of the work function or carrier type of the contact used (e.g., a heavily-doped p-type window layer forms an ohmic tunnel contact with n-type indium tin oxide).

The ni portion of the energy band diagram featured in Fig. 1 is reminiscent of two well-known thin-film solar cells, in which the absorber layer is either copper indium gallium diselenide (CIGS) [1], [2], [3], [4] or cadmium telluride (CdTe) [5], [6], [7]. In modern realizations of these cells, the n-type window layer is not a simple, single layer, as implied by Fig. 1. Rather, each n-type window is actually a much more complex multi-layer which has been carefully optimized over a 30 year period of development. Given this historical insight, it is unlikely that p-layer development, as discussed herein, will be accomplished overnight or will necessarily involve the use of a single p-type layer. However, the rapidity at which p-window layer identification, synthesis, optimization, and integration will be accomplished will undoubtedly benefit greatly from insights obtained in optimizing ni heterojunction thin-film solar cell interfaces.

In the work discussed herein, our primary interest involves materials selection, interface considerations, and initial attempts to integrate p-type window layers into ni single-heterojunction thin-film solar cells in order to realize pin double-heterojunction thin-film solar cells. As evident from a reading of this paper, we have barely scratched the surface with respect to achieving this goal. Many challenges remain regarding basic p-type material selection-optimization, interface design-assessment, and, most notably, p-type layer integration into a solar cell. Perhaps the most intimidating aspect of thin-film solar cell materials development is the fact that the only true test of a constituent solar cell layer is its effect in improving the efficiency, lifetime, and/or cost of a solar cell. Thus, in order to truly validate the viability of a p-type window layer, a complete and optimized solar cell must be fabricated and tested.

This paper is arranged as follows. The next two sections review modern Schottky barrier and heterojunction theory, [8], [9] since this forms the basis of our efforts related to theoretical interface design-assessment. These sections draw heavily on Ref. [9] and references therein,

which should be consulted if a more detailed treatment of these topics is required. Next, several types of metal-semiconductor and heterojunction interfaces are theoretically assessed, and efforts to integrate a specific p-type layer - barium copper tellurium fluoride or BCTF - into CIGS and CdTe thin-film solar cells are detailed. Finally, a few concluding remarks are offered regarding challenges and opportunities with respect to the integration of p-type window layers into thin-film solar cells.

2 Schottky Barrier Theory

Formation of a Schottky barrier between a metal and a p-type semiconductor, as envisaged by ideal Schottky barrier theory from an energy band diagram perspective, is illustrated in Fig. 2. Figure 2(a) shows the metal and p-type semiconductor in isolation and with all relevant material properties referenced to the vacuum level, E_{VAC}. Materials properties of interest to Schottky barrier assessment include the metal work function, Φ_M, the semiconductor work function, Φ_S, the semiconductor electron affinity, χ_S, and the semiconductor ionization potential, IP_S. For the case indicated in Fig. 2, the semiconductor work function, Φ_S, is larger than the metal work function, Φ_M.

As the two materials are brought into intimate contact, Fermi-level-mediated charge transfer, shown as electron transfer from the metal to the semiconductor by the right-going arrow in Fig. 2(a), occurs as the two Fermi levels align. This charge transfer sets up a *macroscopic* dipole at the interface, consisting of a space charge region in the semiconductor of macroscopic dimensions (compared to atomic dimensions) and a sheet of charge at the metal surface, the energy band diagram of which is shown in Fig. 2(b). A built-in potential, V_{BI}, and a corresponding local vacuum level, E_{LVAC}, arise as a consequence of this charge transfer, as indicated in Fig. 2(b). A Schottky barrier, ϕ_{Bp}, also results from this charge transfer and constitutes a potential barrier over which holes in the metal at the Fermi level energy must overcome in order to transit into the semiconductor. The built-in potential, V_{BI}, defines a potential barrier preventing holes at the top of the valence band in the semiconductor bulk from transiting into the metal.

Non-ideal Schottky barrier theory, as illustrated in Figs. 3 and 4, [10] is accomplished by incorporating the charge neutrality level, E_{CNL}, of the semiconductor into the discussion. A charge neutrality level is the branch point within the bandgap of a semiconductor below (above) which interface states are predominately valence (conduction) band derived, or donor-like (acceptor-like) [8], [11]. E_{CNL} can be estimated from band structure calculations [8], [11], [12], [13], [14] or from valence band offset data [8], [15]. The location of the charge neutrality level establishes the nature of additional, non-ideal charge transfer during interface formation, as shown in Figs. 3 and 4.

The direction of the additional non-ideal charge transfer is determined by the position of the charge neutrality level, E_{CNL}, relative to the metal Fermi level, E_F, when these materials are isolated from one another. For the interaction illustrated in Fig. 3(a), E_{CNL} is below the metal Fermi level. Therefore, additional non-ideal electronic charge transfer is directed from the metal to the semiconductor (upper, right-going arrow in Fig. 3(a)), augmenting the ideal Fermi-level-

mediated electronic charge transfer (lower, right-going arrow in Fig. 3(a)). This additional, non-ideal electronic charge transfer results in a reduction of the built-in potential, V_{BI}, and the Schottky barrier height, ϕ_{Bp}, compared to the ideal case, as shown in Fig. 3(b), since this additional charge transfer contributes to the formation of a positive *microscopic* dipole of atomic dimensions.

In Fig. 4 the charge neutrality level, E_{CNL}, is positioned above the metal Fermi level, such that non-ideal electronic charge transfer occurs from the semiconductor to the metal. This leads to an increase in the built-in potential, V_{BI}, and the Schottky barrier height, ϕ_{Bp}, compared to that of the ideal case, due to the formation of a negative *microscopic dipole*, as revealed in Fig. 4(b).

Quantitatively, non-ideal Schottky barrier theory can be conveniently formulated as a one-term correction to ideal Schottky barrier theory. According to non-ideal theory, the Schottky barrier height for a p-type semiconductor, ϕ_{Bp}, can be expressed as

$$\phi_{Bp} = IP_S - \Phi_M - \Delta_{SB}, \tag{1}$$

where Δ_{SB} is the Schottky barrier microscopic dipole correction, accounting for non-ideal charge transfer between the semiconductor charge neutrality level and the metal Fermi level [16]. In Eq. (1), and in other non-ideal Schottky barrier theory equations, ideal Schottky barrier theory is obtained by simply setting Δ_{SB} = 0. Similarly, the Schottky barrier height for an n-type semiconductor, ϕ_{Bn}, (not relevant to the current discussion involving Figs. 2-4, but of interest to the general development of Schottky barrier and heterojunction theory), is given by

$$\phi_{Bn} = \Phi_M - \chi_S + \Delta_{SB}. \tag{2}$$

Additionally, for a metal-semiconductor junction (including the case of a rectifying Schottky barrier and of a non-rectifying ohmic contact; both situations are addressed in the context of what is denoted herein as Schottky barrier theory) the built-in potential for a hole at the top of the semiconductor valence band or for an electron at the bottom of the semiconductor conduction band are equal to

$$V_{BI}^{pSB} = \Phi_S - \Phi_M - \Delta_{SB}, \textit{ and} \tag{3}$$

$$V_{BI}^{nSB} = \Phi_M - \Phi_S + \Delta_{SB}. \tag{4}$$

The Schottky barrier microscopic dipole correction factor, Δ_{SB}, is equal to

$$\Delta_{SB} = (1 - S)\cdot(\Phi_{CNL} - \Phi_M), \tag{5}$$

where S is a Schottky barrier interface parameter, approximated as [8]

$$S = \frac{1}{1 + 0.1(\varepsilon_\infty - 1)^2}, \tag{6}$$

where ε_∞ is the high-frequency relative dielectric constant of the semiconductor. S accounts for dynamic electronic screening at the interface between the metal and the semiconductor.

According to Eq. (5), there are two situations in which $\Delta_{SB} = 0$, such that non-ideal Schottky barrier theory reduces to ideal theory. The first case is obtained when there is no misalignment between E_F and Φ_{CNL}, so that there is no non-ideal charge transfer. The second case occurs in the no-screening limit, when $\varepsilon_\infty \to 1$ so that $S \to 1$.

In contrast, in the perfect-screening limit, $\varepsilon_\infty \to \infty$ so that, according to Eq. (6), $S \to 0$; then, according to Eq. (5), $\Delta_{SB} \to \Phi_{CNL} - \Phi_M$; this means that, using Eq. (1), $\phi_{Bp} \to IP_S - \Phi_{CNL}$; also, from Eq. (3), $V_{BI}^{pSB} \to \Phi_S - \Phi_{CNL}$. This perfect-screening limit is often referred to as constituting `Fermi-level pinning' since the Schottky barrier height and built-in potential are no longer a function of the metal Fermi level position.

Non-ideal Schottky barrier theory will be employed in Section 4 in the assessment of p-layer insertion into CIGS and CdTe thin-film solar cells.

3 HeterojunctionTheory

The pp heterojunction energy band diagrams presented in Fig. 5 are constructed according to ideal heterojunction theory. Although similar in some ways to the ideal-theory energy band diagrams of the p-type Schottky barrier shown in Fig. 2, energy band diagrams for ideal heterojunctions are more complicated in several respects. First, the space charge region extends across the interface, depleting or accumulating both semiconductors instead of just one, as in the Schottky barrier case. This is important because the built-in potential is now dropped across both materials. Second, because voltage is dropped across both materials, the barrier to interfacial carrier transport is defined, to a large extent, in terms of a conduction or valence band discontinuity, shown as ΔE_C and ΔE_V in Fig. 5(b). Overall, similarities between Schottky barrier and heterojunction theory are quite striking. In fact, heterojunction theory is equivalent to Schottky barrier theory in the limit that one of the semiconductors in the heterojunction possesses a carrier concentration approaching that of a metal, as discussed at the end of this section.

Similar to non-ideal Schottky barrier theory, non-ideal heterojunction theory involves charge-neutrality-level-mediated electronic charge transfer across the interface, setting up a *microscopic* interfacial dipole of atomic dimensions. Starting with two isolated semiconductors, ideal (non-ideal) charge transfer occurs between Fermi levels (charge neutrality levels), as shown in Fig. 6(a). Analogous to the non-ideal Schottky barrier cases of Figs. 3-4, non-ideal charge transfer is quantitatively taken into account via the heterojunction microscopic dipole correction factor, Δ_{HJ}, causing the local vacuum level to be discontinuous, as illustrated in Fig. 6(b). This discontinuity modifies conduction and valence band discontinuities compared to what they would be for the ideal-theory case, increasing or decreasing them in magnitude. Additionally, non-ideal charge transfer alters the built-in potential for each semiconductor, increasing or decreasing the width of a space charge region and modifying the sheet charge density within an accumulation region.

For the heterojunction shown in Fig. 6, the directions are opposite for Fermi-level-mediated and charge-neutrality-level-mediated charge transfer. In this case, non-ideal charge transfer leads to an increase in both built-in potentials, the valence band discontinuity, and the conduction band discontinuity compared to that expected from ideal heterojunction theory, due to the presence of a positive microscopic dipole, as evident from a perusal of Fig. 6(b).

An alternative pp heterojunction situation is shown in Fig. 7. In this case, the direction is identical for both Fermi-level-mediated and charge-neutrality-level-mediated charge transfer. Non-ideal charge transfer gives rise to a decrease in both built-in potentials and also in the valence band discontinuity compared to that of the ideal heterojunction theory result due to the presence of a negative *microscopic* dipole, as evident from an assessment of Fig. 7(b). The space

charge region width also decreases as the built-in potential decreases. In the case presented in Fig. 7, the conduction band discontinuity flips from that of a notch to a step, leading to a minimal change in the barrier seen by electrons in semiconductor 2, but a significant decrease in the potential barrier experienced by electrons in semiconductor 1, as shown in Fig. 7(b).

Quantitatively, analogous to the case for non-ideal Schottky barrier theory, non-ideal heterojunction theory differs from ideal heterojunction theory only in the inclusion of a heterojunction microscopic dipole correction factor, Δ_{HJ}. Ideal heterojunction theory formulas are trivially obtained by simply setting Δ_{HJ} to zero. Also note that even though our heterojunction illustrations have been exclusively confined to pp heterojunctions, the non-ideal heterojunction equations presented below are applicable to all heterojunction types (i.e., pp, nn, pn, and np). Thus, according to non-ideal heterojunction theory, the valence and conduction band discontinuity can be expressed as

$$\frac{\Delta E_V}{q} = IP_2 - IP_1 - \Delta_{HJ}, \; and \tag{7}$$

$$\frac{\Delta E_C}{q} = \chi_1 - \chi_2 + \Delta_{HJ}. \tag{8}$$

Furthermore, according to non-ideal heterojunction theory, the built-in potential for holes and for electrons in semiconductor 2 are given by

$$V_{BI}^{pHJ} = \Phi_2 - \Phi_1 - \Delta_{HJ}, \; and \tag{9}$$

$$V_{BI}^{nHJ} = \Phi_1 - \Phi_2 + \Delta_{HJ}. \tag{10}$$

Finally, the heterojunction microscopic dipole correction factor is equal to

$$\Delta_{HJ} = (1 - S_{12})(\Phi_{CNL2} - \Phi_{CNL1}), \tag{11}$$

where S_{12} is a heterojunction interface parameter associated with screening at the interface between both semiconductors, and is estimated as

$$S_{12} = \frac{1}{1 + 0.1\left[\dfrac{(\varepsilon_{\infty 1} - 1)^2 \cdot (\varepsilon_{\infty 2} - 1)^2}{(\varepsilon_{\infty 1} - 1)^2 + (\varepsilon_{\infty 2} - 1)^2}\right]}, \tag{12}$$

where ε_∞ is the high-frequency relative dielectric constant for each respective semiconductor.

As mentioned previously, non-ideal heterojunction theory simplifies to ideal heterojunction theory as $\Delta_{HJ} \to 0$. As evident from Eq. (11), Δ_{HJ} is equal to zero when there is no charge neutrality level misalignment (i.e., when $\Phi_{CNL1} = \Phi_{CNL2}$) or in the no-screening limit (i.e., when either $\varepsilon_{\infty 1} \to 1$ or $\varepsilon_{\infty 2} \to 1$ so that, according to Eq. (12), $S_{12} \to 1$).

Furthermore, if one of the two semiconductors in the heterojunction is strongly degenerately doped, e.g., if $\varepsilon_{\infty 1} \to \infty$, then, according to Eq. (12), $S_{12} \to S_2$; also, since strongly degenerate doping moves the Fermi level deep into one of the bands, certain bandgap-related heterojunction parameters lose their relevance such that $\Phi_{CNL1} \to \Phi_M$, $\Phi_1 \to \Phi_M$, $\chi_1 \to \Phi_M$, $IP_1 \to \Phi_M$, $\Delta E_V \to \phi_{Bp}$, and $\Delta E_C \to \phi_{Bn}$; making notational changes in order to be consistent with Schottky barrier nomenclature: $S_2 \to S$, $\Phi_{CNL2} \to \Phi_{CNL}$, $\chi_2 \to \chi_S$, and $IP_2 \to IP_S$; this

results in Eq. (7) → Eq. (1), Eq. (8) → Eq. (2), Eq. (9) → Eq. (3), Eq. (10) → Eq. (4), Eq. (11) → Eq. (5), and Eq. (12) → Eq. (6). In short, non-ideal heterojunction theory simplifies to non-ideal Schottky barrier theory in the limit of strong degenerate doping of one semiconductor.

Finally, the perfect-screening limit occurs when both $\varepsilon_{\infty 1} \to \infty$ and $\varepsilon_{\infty 2} \to \infty$. Then, from Eq. (12), $S_{12} \to 0$. Consequently, assessment of Eq. (11) leads to $\Delta_{HJ} \to \Phi_{CNL2} - \Phi_{CNL1}$. Subsequent evaluation of Eqs. (7)-(10) results in $\Delta E_V / q \to (IP_2 - \Phi_{CNL2}) - (IP_1 - \Phi_{CNL1})$, $\Delta E_C / q \to (\chi_1 - \Phi_{CNL1}) - (\chi_2 - \Phi_{CNL2})$, $V_{BI}^{pHJ} \to (\Phi_2 - \Phi_{CNL2}) - (\Phi_1 - \Phi_{CNL1})$, and $V_{BI}^{nHJ} \to (\Phi_1 - \Phi_{CNL1}) - (\Phi_2 - \Phi_{CNL2})$. These equations reveal that in the perfect-screening limit, all heterojunction barrier equations are determined by energy differences with respect to charge neutrality levels. Note that this perfect-screening limit situation differs from the strong degenerate doping case considered in the previous paragraph. The perfect-screening limit considered here, and also at the end of the Schottky barrier theory section, is a consequence of dealing with materials possessing exceedingly large high-frequency dielectrics, rather than semiconductors which are subjected to heavy doping so that they become metallic. Thus, for this perfect-screening case, bandgap-related quantities such as χ, IP, and Φ_{CNL}, retain their relevance and do not all collapse into being equal to a metallic Fermi level.

4 p-Layer Insertion

A p-type window material in a pin double-heterojunction thin-film solar cell has two main functions. First, the material is chosen to have a bandgap of adequate width and offset to provide a barrier which helps to suppress recombination of electrons at the anode contact. Second, the material should have a large ionization potential, IP_S, and be strongly p-type, with a very high hole concentration in order to facilitate the formation of an ohmic contact between the absorber and the anode contact.

In the remainder of this section, we will first consider material parameters employed in Schottky barrier and heterojunction calculations. Next, Schottky barrier assessment is accomplished for several types of CIGS, CdTe, and BCTF interfaces. The purpose of this assessment is to elucidate some of the issues involved in obtaining an anode ohmic contact. Finally, we will evaluate several relevant heterojunctions and also describe some initial attempts at p-layer integration into CIGS and CdTe thin-film solar cells.

4.1 Materials Parameters

Relevant semiconductor parameters required for subsequent Schottky barrier or heterojunction assessment are collected in Table 1 as obtained from Refs. [4], [6], [7], [8], [12], [17], [18], [19], [20], [21], [22], [23]. Additionally, the metal work functions used for this analysis are as follows: Al = 4.2 V , Au = 5.32 V, Mo = 4.3 [24]. A few comments are warranted about the perceived accuracy of the materials parameters selected.

All metal work functions are well established. Additionally, all semiconductor materials parameters for CdTe and CIGS appear to be well known, with the possible exception of charge neutrality levels. Parameters for MoSe_2 appear to be relatively well known, again except for the charge neutrality level. Note that the ionization potential for MoSe_2 is estimated electrochemically [21] and that a conversion from the absolute potential scale (referenced to the

standard hydrogen electrode) to the physical scale (referenced to the vacuum level) is accomplished by assuming that the standard hydrogen electrode corresponds to 4.44 eV below the vacuum level [22]. Material parameters for BCTF are not at all well established, since this material is rather new. Materials parameter uncertainties are considered below.

The charge neutrality level energy can be calculated most accurately from an assessment of the complex band structure [12]. Alternatively, it may be estimated theoretically from well-established correlations between the charge neutrality level and the midpoint of the dielectric bandgap using normal band structure calculations [8], [13], [15]. Some disagreement exists in the location of Φ_{CNL} in CdTe. According to Mönch [8], Φ_{CNL} has been calculated from complex band structure theory and estimated from the dielectric bandgap midpoint method, respectively, to be at either 0.85 eV or 1.12 eV above the top of the valence band in CdTe. The 0.85 eV estimate is used in this analysis since the complex band structure calculation is believed to be more accurate. Note that the basic conclusions presented herein do not depend critically on this choice. Φ_{CNL} for CIGS has been estimated from the dielectric bandgap midpoint method in conjunction with empirical tight-binding band structure calculations to be 0.79 eV above the top of the valence band [15]. Charge neutrality levels for $MoSe_2$ and BCTF have not been reported previously. Following Mönch [8], we have calculated Φ_{CNL} for both materials using the dielectric bandgap midpoint method in conjunction with full-potential linearized augmented plane-wave band structure calculations. In these calculations, the local density approximation bandgap is corrected to the experimental value using the scissor operation. We estimate Φ_{CNL} to be 0.43 and 1.30 eV above the valence band maximum for $MoSe_2$ and BCTF, respectively

Relatively few wide-bandgap, p-type semiconductors appropriate for use as p-type thin-film window layers are known to exist [25], [26], [27], [28], [29], [31], [32], [33], [34], [35]. Table 2 is a list of wide-bandgap p-type material candidates. Most of these materials have been only very recently synthesized as powders, dense pellets, and, sometimes, as thin films. Much more work is required before the thin film properties of these materials, as relevant to solar cells, can be considered to have been optimized.

A focus of the remainder of this paper involves exploration of barium copper tellurium fluoride (BaCuTeF, or BCTF) as a p-type insertion layer for pin double-heterojunction thin-film solar cell applications. This material should not be construed as optimal for this purpose. Rather, it is chosen from a materials family with which we have focussed a significant amount of recent research effort [26], [27], [28], [29], [31], such that it was at an appropriate stage of development to be available for this application.

BCTF was initially developed as a transparent p-type conductive material [26], [27], [28], [29], [31]. With a bandgap of 2.3 eV (indirect) and 3.0 eV (direct), a carrier concentration of $\sim 10^{20}$ cm^{-3}, a mobility as large as 8 $cm^2/V \cdot s$, and 70-80 % transparency in the visible portion of the electromagnetic spectrum, [29], [31] BCTF is potentially useful as a p-type insertion layer for the realization of a pin double-heterojunction thin-film solar cell.

Carrier concentration is the only well-established material parameter for BCTF. Multiple conductivity and Hall measurements have reliably shown the carrier concentration of BCTF to be $\sim 10^{20}$ cm^{-3}.

Some uncertainty exists with regard to the bandgap of BCTF [29], [31]. Optical measurements of BCTF indicate a direct bandgap of ~ 3.0 eV. However, a slight yellow coloration of the film and diffuse reflectance measurements of BCTF powders suggest an

indirect bandgap of 2.3 eV. For purposes of this analysis, a bandgap of 2.3 eV is assumed. If a bandgap of 3.0 eV is used and if the ionization potential is assumed to be invariant, the barrier to minority carrier electron back-contact injection increases, a desirable result. Therefore, 2.3 eV is a worst-case estimate for the bandgap of BCTF.

The electron affinity and the ionization potential of BCTF are not known. Our ionization potential estimate for BCTF is based on trends reported by Zhang *et al.* [17] for six copper-based sulfides, selenides, and tellurides (i.e., $CuInS_2$, $CuInSe_2$, $CuInTe_2$, $CuAlSe_2$, $CuGaSe_2$, and $CuIn_5Se_8$). For these materials, the ionization potential is 5.5 $\pm$ 0.3 V with respect to the valence level (assuming the ZnS energy reference to be equal to 6.6 eV, as reported by McCaldin [18]). Thus, the compilation of Zhang *et al.* suggests that the ionization potential of Cu-3d-derived valence bands is approximately 5.5 V. For purposes of this analysis, the ionization potential of BCTF was assumed to be 5.5 V. Note that the ionization potential of various Cu-3d-derived oxides are slightly less than this assumed value of 5.5 V for BCTF (i.e., $IP_S(CuO)$ = 5.42 V [36], $IP_S(CuAlO_2)$ = 5.2 V [37], $IP_S(CuYO_2)$ = 5.3 V [38], $IP_S(CuCrO_2)$ = 5.3 V [39], $IP_S(CuGaO_2)$ = 5.1 V [40], $IP_S(CuFeO_2)$ = 4.9 V [41]). Since recent research has rendered our assumed value of IP_S(BCTF) of questionable accuracy, this issue will be revisited in Section 4.4.

4.2 Schottky Barrier Assessment

Two types of Schottky barrier assessment will be undertaken. First, CIGS-metal and CdTe-metal interfaces will be evaluated in order to demonstrate that it is impossible to form an ohmic anode contact to these layers via the normal approach of simply employing a high work function metal. Next, the BCTF-metal contact will be appraised, since this interface is relevant to p-layer insertion for the realization of pin double-heterojunction thin-film solar cells.

4.2.1 CIGS Interfaces

According to Schottky barrier theory, as described in Section 2, it is impossible to form an ohmic anode contact to CIGS using a high work function metal.

In order to begin to see this, consider the energy band diagrams indicated in Fig. 8, which describe the molybdenum-CIGS interface. As evident from an inspection of Fig. 8(a), both ideal and non-ideal charge transfer are directed from the metal to the semiconductor, as is indicated by the right-going arrows. Right-going, non-ideal charge transfer or, equivalently, a positive *microscopic* dipole [42], works to significantly reduce the Schottky barrier height, ϕ_{Bp}, from 1.35 V (ideal theory) to 0.87 V (non-ideal theory). However, according to both ideal and non-ideal theory, the predicted Schottky barrier height is so large that formation of an ohmic contact is precluded using molybdenum as an anode contact metal [43].

Next, Fig. 9 exhibits energy band diagrams for the gold-CIGS interface. Since gold has a work function of 5.32 V compared to the 4.3 V work function of molybdenum, it would be expected that using a material with this large of a work function would significantly reduce the Schottky barrier height. However, according to non-ideal theory, this is not the case since $\phi_{Bp}(Au)$ = 0.73 V (0.33 V) compared to $\phi_{Bp}(Mo)$ = 0.87 V (1.35 V) [ideal theory values are

shown in parentheses]. Note that for $\phi_{Bp}(Au)$ the ideal theory value is smaller than that of the non-ideal theory, while this trend is reversed for $\phi_{Bp}(Mo)$. This trend reversal is a consequence of the fact that non-ideal charge transfer is right-going from the metal to the semiconductor in Fig. 8 (giving rise to a positive *microscopic* dipole, which reduces ϕ_{Bp}) while it is left-going from the semiconductor to the metal in Fig. 9 (giving rise to a negative *microscopic* dipole, which increases ϕ_{Bp}). Additionally, and more importantly, the interface parameter, S, which characterizes the extent of interfacial screening between the metal and the semiconductor surface, is very small, i.e., S = 0.14 for CIGS. This means that only 14% of the metal work function difference between Mo and Au is effective in modifying the Schottky barrier height, ϕ_{Bp}.

Performing the following calculation is a more dramatic way to use Schottky barrier theory to reveal that it is impossible to form an ohmic anode contact to CIGS using a high work function metal. Formation of an ohmic anode contact ideally requires the Schottky barrier height to be zero or negative, i.e., $\phi_{Bp} \leq 0$. Thus, it is necessary to use Schottky barrier theory to calculate an appropriate value of Φ_M which will ensure that $\phi_{Bp} \leq 0$. To do this, substitute Eq. (5) into Eq. (1), and then solve for the metal work function required to make $\phi_{Bp} \leq$ 0. This yields

$$\Phi_M(\phi_{Bp} \leq 0) \geq (1-1S)\Phi_{CNL} + IP_S S. \tag{13}$$

For CIGS, this results in $\Phi_M(\phi_{Bp} \leq 0) \geq$ 10.5 V. This work function is significantly larger than that of any known contact material.

Thus, the essential point here is that it is impossible to make an ohmic anode contact to CIGS using a high work function metal. This impossibility is primarily a consequence of CIGS having a very small interface parameter, S, so that only an extremely small fraction of the extra metal work function is effective in decreasing the Schottky barrier height, ϕ_{Bp}. Having a small S corresponds to having significant interfacial screening between the metal and the semiconductor.

4.2.2 CdTe Interfaces

According to Schottky barrier theory, it is also impossible to form an ohmic anode contact to CdTe using a high work function metal. The situation is similar to the one just encountered for CIGS.

Consider the energy band diagrams indicated in Fig. 10, which describe the gold-CdTe interface. This situation is quite similar to the gold-CIGS interface case given in Fig. 9. Most notably, the upper, left-going arrow in Fig. 10 is indicative of non-ideal charge transfer (negative *microscopic* dipole) which significantly increases the Schottky barrier height, ϕ_{Bp}, from 0.46 V (ideal theory) to 0.77 V (non-ideal theory). In both the ideal and non-ideal theory cases, the Schottky barrier height is predicted to be so large that ohmic contact formation is not possible.

Since the interface parameter for CdTe is slightly better than that for CIGS, i.e., S(CdTe) = 0.21 compared to S(CIGS) = 0.14, the anode ohmic contact situation is marginally improved. However, performing the same calculation as described in Section 4.2.1 using Eq. (13) leads to $\Phi_M(\phi_{Bp} \leq 0) \geq$ 8.9 V, still an impracticably large value. Thus, it is impossible to make an ohmic anode contact to CdTe using a high work function metal.

Given that we have twice encountered attractive solar cell absorbers, i.e., CIGS and CdTe, in which anode ohmic contact formation is problematic, it seems worthwhile to pose the following question: What materials properties are most suitable for achieving a good anode ohmic contact, within the context of Schottky barrier theory?

Forming a good anode ohmic contact requires ensuring that efficient hole transport occurs across the metal-semiconductor interface in both directions, from metal to semiconductor and from semiconductor to metal. This is accomplished most effectively when the hole built-in potential, V_{BI}^{pSB}, and the Schottky barrier height, ϕ_{Bp}, are restricted as follows

$$V_{BI}^{pSB} \leq 0, and\ \phi_{Bp} \leq IP_S - \Phi_S. \tag{14}$$

The second inequality simply recognizes that the separation of the Fermi level and E_V in the semiconductor bulk constitutes a minimum barrier between the metal Fermi level and E_V in the bulk of the semiconductor after interface formation (see Fig. 2, for example, for clarification). Substituting Eqs. (1) and (3) into Eq. (14) and rearranging yields

$$\Phi_S - \Phi_M \leq \Delta_{SB}. \tag{15}$$

Note that the two inequalities given in Eq. (14) lead to the same constraining inequality, as indicated in Eq. (15).

Equation (15) specifies conditions for achieving anode ohmic contacts. This inequality is most readily satisfied if the quantity to the left is negative while the quantity on the right, Δ_{SB}, is positive. Thus, Eq. (15) suggests that ohmic anode contacts are most favorably formed when (i) $\Phi_S \leq \Phi_M$ (corresponding to negative *macroscopic* dipole formation), and using Eq. (5), (ii) $\Phi_M \leq \Phi_{CNL}$ (corresponding to positive *microscopic* dipole formation). Note that (ii) reveals that a p-type absorber possessing a band structure which positions Φ_{CNL} near to the top of the valence band is advantageous for facilitating ohmic contact formation.

4.2.3 BCTF Interfaces

Since BCTF is to be employed as a p-type insertion layer, it is appropriate to evaluate the nature of the metal-BCTF interface formed when it is contacted on its backside, i.e., on the side opposite to the absorber layer. This assessment is accomplished using aluminium as the contact metal, since this is what was used in our integration experiments. Moreover, the actual metal used is non-critical, as is evident from the following discussion.

Energy band diagrams illustrating the aluminium-BCTF interface are shown in Fig. 11. At first glance, Fig. 11 looks very similar to Figs. 8 and 10, in that the Schottky barrier height, ϕ_{Bp}, is extremely large (i.e., 1.30 V), which appears to preclude the realization of an ohmic contact. However, upon further inspection, it is clear that the depletion layer thickness is minuscule (i.e., 3.8 nm) compared to the depletion layers of Figs. 8 and 10. This dramatic reduction is a consequence of the fact that the hole concentration in BCTF is extremely large compared to CIGS or CdTe, i.e., p(BCTF) ~ 10^{20} cm^{-3} compared to ~ 10^{16} cm^{-3} for CIGS and CdTe. The important message to be learned from Fig. 11 is that the high hole concentration in BCTF makes the depletion layer so thin that the large Schottky barrier height is inoperative in impeding carrier transport between aluminium and BCTF since interfacial carrier transport is accomplished via tunneling.

Thus, the aluminium-BCTF interface constitutes an ohmic tunneling contact.

One additional aspect of Fig. 11 merits comment. Φ_M and Φ_{CNL} are aligned at 4.2 V such that there is no charge neutrality mediated non-ideal charge transfer. Thus, for this situation, ideal and non-ideal Schottky barrier theory predictions are identical.

4.3 Heterojunctions

Heterojunction assessment related to p-layer insertion of BCTF into CIGS and CdTe thin-film solar cells is presented. Two attempts at BCTF p-layer insertion are briefly described. Also, the CIGS-$MoSe_2$-Mo interface is analyzed from the combined perspective of Schottky barrier and heterojunction theory.

4.3.1 CIGS Interfaces

Energy band diagrams for the BCTF-CIGS heterojunction are illustrated in Fig. 12. Notice that this interface is ohmic, as evident from the upward interfacial band-bending of the valence band and the small interfacial barrier.

Another way to recognize that this is an ohmic contact is to evaluate the sign of the built-in potential for the carrier of interest, in this case holes. This leads to V_{BI}^{pHJ} = -0.60 V (-0.21 V), which means that both the non-ideal and ideal (in parentheses) hole barriers in the CIGS are negative, indicating that they are ohmic. Alternatively, note that V_{BI}^{nHJ} = +0.60 V (+0.21 V), indicating that the band-bending in the CIGS near the interface presents a barrier for electrons in the CIGS, inhibiting their transport into the BCTF.

In this case, however, V_{BI}^{nHJ} does not reveal the true nature and magnitude of the interfacial electron barrier, as evident from an assessment of Fig. 12. To a large extent, the CIGS electron barrier is established by the conduction band discontinuity, ΔE_C = -0.91 V (-1.30 V). The large magnitude of ΔE_C is indicative of a large electron barrier. The negative sign associated with ΔE_C is likely to be confusing. The polarity of ΔE_C is established by the conduction band discontinuity induced interfacial barrier which a conduction band electron at ΔE_C sees when it travels from BCTF into CIGS. The absence of a conduction band interfacial barrier from BCTF into CIGS in the energy band diagram of Fig. 12b indicates that this is a 'negative barrier'.

Once again, note that the BCTF-CIGS heterojunction interface shown in Fig. 12 is ohmic, as desired. Two factors contribute to favoring the use of a heterojunction rather than a metal-semiconductor interface for the realization of an anode ohmic contact.

First, the work function of the `metal', i.e., the heavily-doped, p-type wide-bandgap semiconductor, may be chosen to be larger than that of a conventional metal contact. This is due to the fact that ionization potentials for certain wide-bandgap semiconductors are larger than that of the largest known metal work function (i.e., Φ_M (Pt) = 5.4 V [24]). Furthermore, if the p-type wide-bandgap semiconductor is strongly degenerately doped, the work function of this material is actually larger than its ionization potential.

Second, as indicated in Fig. 12, non-ideal charge transfer appears to favor a right-going transfer (positive *microscopic* dipole) from BCTF to CIGS, since the BCTF charge neutrality

level is positioned above that of CIGS. Similar to the case discussed in Section 4.2.1 with respect to CIGS Schottky barrier interfaces, right-going non-ideal charge transfer or, equivalently, a positive *microscopic* dipole, aids in the formation of an ohmic anode contact.

A quantitative treatment of anode ohmic contact formation from a heterojunction perspective may be accomplished as follows. This assessment assumes that semiconductor 1 is the heavily-doped p-window and semiconductor 2 is the lightly-doped p-absorber. From a heterojunction perspective, forming a good p-type ohmic contact requires restricting the hole built-in potential, V_{BI}^{pHJ}, and the valence band discontinuity, $\Delta E_V / q$, as follows

$$V_{BI}^{pHJ} \leq 0, and\ \Delta E_V q \leq (IP_2 - \Phi_2) - (IP_1 - \Phi_1). \tag{16}$$

The second inequality recognizes that the minimum valence band discontinuity is established by bulk Fermi level to E_V separations for both semiconductors (see Fig. 5, for example, for clarification). Substituting Eqs. (7) and (9) into Eq. (16) and rearranging yields

$$\Phi_2 - \Phi_1 \leq \Delta_{HJ}. \tag{17}$$

Note that the two inequalities given in Eq. (16) lead to the same constraining inequality, as indicated in Eq. (17). Equation (17) specifies conditions for achieving heterojunction anode ohmic contacts. This inequality is most readily satisfied if the quantity to the left is negative while the quantity on the right, Δ_{HJ}, is positive. Thus, Eq. (17) suggests that ohmic anode contacts are most favorably formed when (i) $\Phi_2 \leq \Phi_1$ (corresponding to negative *macroscopic* dipole formation), and using Eq. (11), (ii) $\Phi_{CNL1} \leq \Phi_{CNL2}$ (corresponding to positive *microscopic* dipole formation). This situation is directly analogous to the Schottky barrier anode ohmic contact assessment considered in Section 4.2.2.

Several attempts were made to integrate a p-type BCTF window layer into a CIGS solar cell. This was accomplished by depositing (via pulsed laser deposition at a substrate temperature of 550 $^\circ$C) a 40 nm thick layer of BCTF onto Mo- or ITO-coated glass slides at Oregon State University and then shipping these back-contacted samples to the University of Delaware for completion of the CIGS solar cell (i.e., 2 μm or 0.7 μm of CIGS at 550 $^\circ$C, 0.05 μm of CdS, 0.05 μm of ZnO (high resistance at the CdS-ZnO interface, transitioning to low resistance at the surface), 0.15 μm of ITO, and 3 μm of a patterned Ni-Al contact metallization) and characterization. None of these BCTF integration attempts were particularly successful. The performance of control samples, i.e., Mo-back-contacted devices with and without BCTF insertion layers, were clearly degraded when BCTF was introduced. BCTF insertion arguably improved the performance of samples fabricated on ITO-coated glass substrates, but the performance of these devices was always poor. This poor performance is partially due to the fact that that sodium-free glass substrates were employed.

Scanning electron microscope (SEM) images of BCTF/ITO interfaces, as shown in Fig. 13, provide insight into a fundamental problem associated with this BCTF insertion experiment. Figure 14(a) shows a BCTF/ITO interface after a 550 $^\circ$C post-deposition anneal in an argon ambient; this corresponds to the temperature at which CIGS is deposited. The BCTF layer can clearly be seen, confirming that the BCTF/ITO interface is compatible with an

annealing temperature of 550 $^{\circ}$C. In contrast, in Fig. 14(b) there is no evidence of the BCTF layer after CIGS processing, suggesting that the BCTF constituents have inter-diffused into the CIGS film during CIGS deposition. In conclusion, it appears that BCTF cannot withstand the process conditions required for the deposition of CIGS. Thus, exploration of BCTF as a p-type window layer needs to be pursued using a different thin-film solar cell materials system.

Recall from the discussion presented in Section 4.2.1 that according to Schottky barrier theory it is impossible to form an ohmic anode contact to CIGS using a high work function metal. However, it is well-known [1], [2], [3], [4] that formation of $MoSe_2$ at the molybdenum-CIGS interface facilitates achievement of an ohmic anode contact.

To see how this occurs, consider the energy band diagrams presented in Fig. 14. This figure is more complicated than any set of energy band diagrams which we have encountered up to now, since it involves the concomitant formation of two interfaces - a Mo-$MoSe_2$ metal-semiconductor interface and a $MoSe_2$-CIGS heterojunction.

First, separately inspect the two interfaces shown in Fig. 14. The Mo-$MoSe_2$ interface is clearly a Schottky barrier, with a large barrier, ϕ_{Bp}^{pSB} = 0.47 V (1.60 V). Even though the right-going, non-ideal charge transfer (positive *microscopic* dipole) dramatically reduces the interfacial barrier height, this interface may be clearly categorized as a rectifying Schottky barrier. In contrast, the $MoSe_2$-CIGS interface is essentially ohmic since the valence band discontinuity is small enough, ΔE_V = 0.26 V (-0.25 V), that it does not present an appreciable impediment to hole transfer across the interface.

Next, note that although the energy band diagrams indicated in Fig. 14 are drawn using the same Schottky barrier and heterojunction theory described previously in Sections 2 and 3, an artificial feature of the energy band diagram presented in Fig. 14(b) is the implicit thickness of the $MoSe_2$ layer. For an assumed $MoSe_2$ p-type carrier concentration of : 10^{17} cm^{3}, the zero-bias depletion region present in the $MoSe_2$ near the Mo-$MoSe_2$ interface would be approximately 75 nm thick, suggesting that the implicit thickness of the $MoSe_2$ layer shown in Fig. 14(b) would be : 200 nm.

In reality, the adventitious $MoSe_2$ layer which is formed at the interface as an unintentional consequence of solar cell fabrication is probably much thinner than this, perhaps ~3-5 nm thick. Thus, to envisage what the actual Mo-$MoSe_2$-CIGS energy band diagram might really look like, one must shrink the thickness of the intermediate $MoSe_2$ layer shown in Fig. 14(b) by a factor of approximately 50. To first order, we propose that the $MoSe_2$-CIGS interfacial barrier will remain basically as it is shown in Fig. 14(b), but will move very close to the Mo-$MoSe_2$ interface, thereby extinguishing much of the depletion region shown near this interface in Fig. 14(b). Additionally, the valence band profile across the entire $MoSe_2$ layer should possess negative curvature, since Fig. 14(a) shows that all Fermi-level- and charge-neutrality-level-mediated charge transfer is directed into this very thin layer.

Thus, the picture which emerges is that ohmic contact formation arises as a consequence of barrier reshaping at the $MoSe_2$-CIGS heterojunction interface together with having the adventitious $MoSe_2$ layer so thin that tunneling occurs across the Mo-$MoSe_2$ interface, even though its interfacial barrier height is quite large.

4.3.2 CdTe Interfaces

Since the substrate configuration (i.e., anode contact at the bottom of the stack) of a CIGS solar cell appears to be incompatible with BCTF p-layer insertion, several attempts were made to integrate BCTF into a CdTe superstrate cell (i.e., anode contact at the top of the stack). Prior to discussing these BCTF integration attempts, energy band diagrams for this anode contact are presented, once again as derived from Schottky barrier and heterojunction theory of Sections 2 and 3.

Figure 15 shows energy band diagrams corresponding to the formation of an Al-BCTF-CdTe interface. This figure is similar to Fig. 14, in that BCTF-CdTe heterojunction and Al-BCTF metal-semiconductor formation are shown simultaneously. According to the energy band diagram of Fig. 15(b), the Al-BCTF-CdTe interface should function as an ohmic contact since ΔE_V = -0.12 V (0.28 V) and V_{BI}^{pHJ} = -0.56 V (-0.16 V). Note that even though a Schottky barrier with a large barrier height, i.e., ϕ_{Bp} = 1.30 V, exists at the Al-BCTF interface, this interface is also ohmic because BCTF is degenerately doped, allowing for easy hole tunneling across the interface.

Attempts to integrate BCTF layers into CdTe solar cells were undertaken by procuring ITO-ZnO-CdS-CdTe substrates from the University of Toledo. Many attempts to introduce a p-type BCTF insertion layer were undertaken. BCTF layers were deposited onto `as received' CdTe surfaces and also onto freshly etched CdTe surfaces. None of these attempts were particularly promising. A significant problem encountered involved time-dependent degradation of the quality of the CdTe surface, which is attributed to the use of a final post-deposition $CdCl_2$ treatment of the surface in the presence of oxygen. Efforts to minimize this problem involving vacuum packing and sample storage inside a nitrogen glovebox were unsuccessful. It appears that successful formation of a high-quality CdTe ohmic anode contact requires formation of this contact immediately after the last post-deposition treatment. In any event, attempts to integrate p-type BCTF window layers into CdTe solar cells were terminated once it was recognized that our initial estimate of the BCTF ionization potential was possibly incorrect.

4.4 BCTF Ionization Potential Reassessment

As discussed in Section 4.1, we selected a value of IP_S(BCTF) = 5.5 V for our BCTF-related Schottky barrier and heterojunction analysis, consistent with previously reported trends for copper-based materials [17], [36], [37], [38], [39], [40], [41]. However, recent photoemission measurements of other members of the BaCuQF (Q = S,Se,Te) family provide evidence that IP_S(BCTF) actually may be significantly smaller than our assumed value of 5.5 V. Specifically, the ionization potential of BaCuSF and BaCuSeF have been reported to be 4.6 and 3.9 eV, respectively [28]. Extrapolating these values, assuming a smaller ionization potential for a tellurium-containing isoelectronic compound, leads to an ionization potential estimate of 3.2 eV. If IP_S(BCTF) is indeed dramatically smaller than 5.5 eV, as suggested by the work of Yanagi et al. [28], BCTF is not an attractive p-type anode insertion layer for pin double-heterojunction thin-film solar cell applications. For example, assuming that IP_S(BCTF) = 3.2 eV, leads to

predictions of ΔE_V /q = 0.71 V instead of -0.24 V for the BCTF-CIGS interface and of ΔE_V /q = 0.91 V instead of -0.12 V for the BCTF-CdTe interface.

Although future work is required to conclusively establish IP_S(BCTF), Yanagi et al.'s photoemission trends, preliminary band structure calculations, and chemical trends all argue that IP_S(BCTF) is significantly smaller than what we assumed in our original development of BCTF and in the interface analysis presented herein. If IP_S(BCTF) turns out to be very small, i.e. ~3.2 V, then BCTF clearly is not an appropriate choice for pin double-heterojunction thin-film solar cell applications. Regardless of the actual value for IP_S(BCTF), the Schottky barrier and heterojunction assessment strategy presented in this paper is still applicable to the elucidation of the interface properties of a generic, but as yet unspecified wide-bandgap, large ionization potential p-type insertion layer. This IP_S(BCTF) controversy underscores the importance of selecting a wide-bandgap, strongly p-type material with a large ionization potential for p-type anode insertion into pin double-heterojunction thin-film solar cells.

5 Conclusions

Modern Schottky barrier and heterojunction theory are employed in an attempt to elucidate interfacial formation issues related to the incorporation of a p-type window layer to form a pin double-heterojunction thin-film solar cell. This p-type window layer serves as an electron reflector and also aids in the formation of an ohmic anode contact. Ohmic anode contacts are particularly difficult to form in CIGS and CdTe thin-film solar cells since these materials have very large ionization potentials, i.e., IP_S = 5.65 (CIGS) and 5.78 V (CdTe) and significant interfacial screening, characterized by extremely small Schottky barrier interface parameters, i.e., S = 0.14 (CIGS) and 0.21 (CdTe). An ideal p-type window material would be heavily-doped, p-type, and would have a wide bandgap, a large ionization potential, and a smaller charge neutrality level energy than that of the absorber.

Insertion of a wide bandgap p-window layer into an ni single-heterojunction structure to realize a pin double-heterojunction solar cell could potentially improve the performance of such a cell. Improvements are anticipated to occur as a consequence of the improved anode ohmic contact and electron reflecting barrier properties. Additionally, a p-window insertion layer offers greater solar cell design flexibility. This improved flexibility is associated with the possibility of reducing the thickness of the absorber, thereby establishing a built-in field across this layer. Without a p-window, the high anode effective surface recombination velocity makes it impractical to significantly reduce the absorber layer thickness. The ability to arbitrarily adjust an absorber layer thickness without unacceptably degrading its anode interface recombination properties could prove useful in future thin-film solar cell design work, especially with regard to the development of tandem cells.

Numerous challenges remain before p-window layer insertion reaches a state of maturity appropriate for its commercialization. These include identification of appropriate materials, process integration, optimization, and solar cell validation.

The application of modern Schottky barrier and heterojunction theory, as presented herein, may aid p-window layer insertion efforts. This theory can be beneficially employed if the following minimal set of p-window layer materials parameters are known (assuming that other relevant absorber and contact material parameters are already available): the hole concentration,

p, the high-frequency dielectric constant, ε_∞, the bandgap, E_G, the electron affinity, χ_S, and the charge neutrality level, Φ_{CNL}. Of these parameters, p, ε_∞, and E_G may be empirically assessed in a rather straightforward fashion. χ_S estimation requires somewhat more specialized equipment, but its measurement is also readily accomplished experimentally once an appropriate sample is available. Φ_{CNL} is clearly the most difficult material parameter to estimate, usually necessitating calculation of the complex band structure. Fortunately, such calculations are now feasible, if computer time-intensive.

Acknowledgements

This work was funded by the National Renewal Energy Laboratory subcontract no. XAT-4-33624-11.

References

[1] U. Rau and H. W. Schock, in Clean Energy from Photovoltaics, edited by M. D. Archer and R. Hill (Imperial College Press, London, 2001), p. 277.

[2] W. N. Shafarman and L. Stolt, in Handbook of Photovoltaic Science and Technology, edited by A. Luque and S. Hegedus (Wiley, Chichester, 2003), p. 567.

[3] R. Klenk, M C. Lux-Steiner, in Thin Film Solar Cells, edited by J. Poortmans and V. Arkhipov (Wiley, Chichester, 2006), p. 237.

[4] S. Siebentritt and U. Rau (Eds.) , Wide-Gap Chalcopyrites, (Springer, Berlin, 2006).

[5] D. Bonnet, in Clean Energy from Photovoltaics, edited by M. D. Archer and R. Hill (Imperial College Press, London, 2001), p. 245.

[6] B. E. McCandless and J. R. Sites, in Handbook of Photovoltaic Science and Technology, edited by A. Luque and S. Hegedus (Wiley, Chichester, 2003), p. 617.

[7] M. Burgelman, in Thin Film Solar Cells, edited by J. Poortmans and V. Arkhipov (Wiley, Chichester, 2006), p. 277.

[8] W. Mönch, Semiconductor Surfaces and Interfaces, 3rd Ed. (Springer, Berlin, 2001).

[9] J. F. Wager, Thin Solid Films 516 (2008) 1755.

[10] Construction of an energy band diagram for a metal-semiconductor interface according to non-ideal Schottky barrier theory is accomplished as follows. First, energy band diagrams for materials in isolation and after interface formation are drawn according to ideal Schottky barrier theory. Next, the Schottky barrier microscopic dipole correction, Δ_{SB}, is calculated using Eq. (5). This dipole correction modifies the local vacuum level, E_{LVAC}, at the interface, causing it to be

discontinuous. If Δ_{SB} is positive, corresponding to right-going non-ideal charge transfer, e.g., as shown in Fig. 3(a), then Δ_{SB} is sketched as an upward-pointing interfacial arrow, as shown in Fig. 3(b). Alternatively, if Δ_{SB} is negative, corresponding to left-going non-ideal charge transfer, e.g., as shown in Fig. 4(a), then Δ_{SB} is sketched as a downward-pointing interfacial arrow, as shown in Fig. 4(b). Regardless of whether Δ_{SB} is positive or negative, the semiconductor side of E_{LVAC} is connected to the head of the arrow corresponding to Δ_{SB}, while the metal side of E_{LVAC} is connected to the tail of the arrow corresponding to Δ_{SB}, and the corresponding modification of the E_{LVAC} due to the Δ_{SB}-induced discontinuity is sketched, e.g., as a dotted line in Figs. 3(b) and 4(b). Finally, the conduction band minimum, E_C, and valence band maximum, E_V, profiles are also easily sketched since their band-bending trend is identical to that of E_{LVAC}. The same basic energy band construction procedure is employed for heterojunctions, except that Δ_{SB} is replaced by the heterojuction microscopic dipole correction, Δ_{HJ}, as given by Eq. (11), and band-bending may occur on both sides of the interface for this somewhat more complicated situation.

[11] J. R. Robertson, J. Vac. Sci. Technol. B 18 (2000) 1785.

[12] J. Tersoff, Phys. Rev. Lett. 52 (1984) 465.

[13] M. Cardona and N. E. Christensen, Phys. Rev. B 35 (1987) 6182.

[14] A. A. Demkov, L. R. C. Fonseca, E. Verret, J. Tomfohr, O. F. Sankey, Phys. Rev. B 71 (2005) 195306.

[15] W. Mönch, in Wide-Gap Chalcopyrites, edited by S. Siebentritt, U. Rau, (Springer, Berlin, 2006), p. 9.

[16] H. Va'zquez, W. Gao, F. Flores, A. Kahn, Phys. Rev. B 71 (2005) 041306.

[17] S. B. Zhang, S.-H. Wei, and A. Zunger, J. Appl. Phys. 83 (1998) 3192.

[18] J. O. McCaldin, Prog. Sol. St. Chem. 26 (1998) 241.

[19] A. M. Vora, Cryst. Res. Tech. 42 (2007) 286.

[20] T. Sekine, M. Izumi, T. Nakashizu, K. Uchinokura, E. Matsuura, J. Phys. Soc. Jpn. 49 (1980) 1069.

[21] H. Gerischer, in Solar Energy Conversion, (Springer-Verlag, Berlin, 1979).

[22] S. Trasatti, Pure & Appl. Chem. 58 (1986) 955.

[23] A.O. Pudov, M. Gloeckler, S.H. Demtsu, J.R. Sites, K.L. Barth, R.A. Enzenroth, W.S. Sampath, 29th IEEE Photovoltaic Specialists Conference (2002) 760.

[24] J. A. Dean (Ed), Lange's Handbook of Chemistry, 15th Ed. (McGraw-Hill, New York, 1999).

[25] S. Park, D. A. Keszler, M. M Valencia, R. L. Hoffman, J. P. Bender, J. F. Wager, Appl. Phys. Lett. 80 (2002) 4393.

[26] H. Yanagi, J. Tate, S. Park, C.-H. Park, D. A. Keszler, Appl. Phys. Lett. 82 (2003) 2814.

[27] H. Yanagi, S. Park, A. D. Draeseke, D. A. Keszler, J. Tate, J. Solid State Chem. 175 (2003) 34.

[28] H. Yanagi, J. Tate, S. Park, C.-H. Park, D. A. Keszler, M. Hirano, H. Hosono, Appl. Phys. Lett. 100 (2006) 083705.

[29] R. Kykyneshi, D. H. McIntyre, J. Tate, C.-H. Park, D. A. Keszler, Solid State Sci. (2008) IN PRESS.

[30] J. Tate (private communication).

[31] J. Tate, P. F. Newhouse, R. Kykyneshi, P. A. Hersh, J. Kinney, D. H. McIntyre, D. A. Keszler, Thin Solid Films 516 (2008) 5795.

[32] H. Hiramatsu, M. Orita, M. Hirano, K. Ueda, H. Hosono, J. Appl. Phys. 91 (2002) 9177.

[33] H. Hiramatsu, K. Ueda, K. Takafuji, H. Ohta, M. Hirano, T. Kamiya, H. Hosono, J. Mater. Res. 19 (2004) 2137.

[34] H. Hiramatsu, K. Ueda, H. Ohta, M. Hirano, M. Kikuchi, H. Yanagi, T. Kamiya, H. Hosono, Appl. Phys. Lett. 91 (2007) 012104.

[35] M. L. Liu, L. B. Wu, F. Q. Huang, L. D. Chen, J. A. Ibers, J. Sol. St. Chem. 180 (2007) 62.

[36] F. P. Koffyberg, F. A. Benko, J. Appl. Phys. 53 (1982) 1173.

[37] F. A. Benko, F. P. Koffyberg, J. Phys. Chem. Sol. 45 (1984) 57.

[38] F. A. Benko, F. P. Koffyberg, Can. J. Phys. 63 (1985) 1306.

[39] F. A. Benko, F. P. Koffyberg, MRS Bull. 21 (1986) 753.

[40] F. A. Benko, F. P. Koffyberg, Phys. Stat. Sol. A 94 (1986) 231.

[41] F. A. Benko, F. P. Koffyberg, J. Phys. Chem. Sol. 48 (1987) 431.

[42] Unless care is taken, signs (i.e., + and -), polarities (i.e., positive and negative) and directions (i.e., right-going and left-going) used in the context of the Schottky barrier-heterojunction theory formulation presented in Sections 2 and 3 can be somewhat confusing. Coherent use of this theory, as enscapsulated in Eqs. (1)-(12), requires sketching energy band diagrams in a consistent manner; for a metal-semiconductor interface, the metal should be positioned to the left; for a heterojunction, semiconductor 1 should be postioned to the left. When these conventions are employed, all interfacial discontinuity barriers are defined with respect to the material positioned to the left (i.e., the metal in the case of Schottky barrier theory, and semiconductor 1 in the case of heterojunction theory), built-in potentials are defined with respect to the space charge region barrier of the material positioned to the right (i.e., the semiconductor in the case of Schottky barrier theory, and semiconductor 2 in the case of heterojunction theory), and dipoles are defined in the direction of negative (electron) charge transfer, with right-going corresponding to a positive quantity.

[43] There are three ways to assess whether a metal-semiconductor interface constitutes an ohmic (low-barrier) or rectfying (high-barrier or Schottky barrier) contact. First, it can be discerned through examination of an energy band diagram by establishing whether majority carriers in the bulk semiconductor see an appreciable interfacial barrier, or, alternatively, a very small or completely absent interfacial barrier. Second, an ohmic contact will have either a negative majority carrier Schottky barrier height or a very small (less than : 0.25 V) positive majority carrier Schottky barrier height. Third, for an ohmic contact, the majority carrier built-in potential will be either negative or positive but very small. Note that Eqs. (3) and (4) for the built-in potential are identical in magnitude and only differ in sign. This is a consequence of the fact that when a barrier is present for one carrier type, it is absent for the other carrier type.

[44] In general, for both metal-semiconductor interfaces and for heterojunctions, it is desirable to have as large of a screening factor, i.e., S or or S_{12}, as possible. Although the Schottky barrier screening situation is quite grim for the materials listed in Table 1, i.e., S = 0.14, 0.21, 0.35, and 0.03 for CIGS, CdTe, BCTF, and $MoSe_2$, respectively, this problem is not as severe when these materials are employed as heterojunctions since heterojunction screening is modeled as capacitors in series in the denominator of Eq. (12). Thus, S_{12} is always larger than either S_1 or S_2. For example S_{12} = 0.41, 0.45, and 0.16 for, respectively, the BCTF-CIGS, BCTF-CdTe, and $MoSe_2$-CIGS interface.

Table 1: Semiconductor materials parameters used for estimation of energy band diagrams for CIGS and CdTe anode contact interfaces. [*Parameters*: p = approximate hole carrier concentration, ε_∞ = high-frequency relative dielectric constant, S = Schottky barrier interface parameter, E_g = bandgap, χ_S = electron affinity, Φ_S = work function (calculated as the Fermi level separation from IP_S using p and assuming a valence band density of states, $N_V = 10^{19}$ cm^{-3}), IP_S = ionization potential, Φ_{CNL} = charge neutrality level]

Material	p (cm^{-3})	ε_∞	S	E_g (eV)	χ_S (V)	Φ_S (V)	IP_S (V)	Φ_{CNL} (V)
CIGS	10^{16}	8.8	0.14	1.15	4.50	5.46	5.65	4.86
CdTe	3×10^{14}	7.1	0.21	1.50	4.28	5.51	5.78	4.93
BCTF	10^{20}	5.3	0.35	2.30	3.20	5.67	5.50	4.20
$MoSe_2$	10^{17}	18.4	0.03	1.20	4.70	5.70	5.90	5.47

References: Φ_{CNL} for BCTF and $MoSe_2$ are obtained from calculations performed in this work. CIGS = Ref. [4]. CdTe = Ref. [23] for p; Ref. [12] for Φ_{CNL}; otherwise Ref. [6]. BCTF = Ref. [29] for p, ε_∞, and E_G; Ref. [17], [18] for IP_S (estimated from copper-based sulfide, selenide, and telluride trends). $MoSe_2$ = Ref. [19] for p and E_G; Ref. [20] for ε_∞; Ref. [21], [22] for IP_S.

Table 2: A summary of candidate materials for p-layer insertion into pin double-heterojunction thin-film solar cells. Barium copper telluride fluoride (BaCuTeF, or BCTF) is exclusively employed in the p-layer insertion assessment and integration work discussed herein.

Material	E_G (eV)	p (cm^3)	Form	μ_{Hall} ($cm^{-2} V^{-1} s^{-1}$)	Reference
BaCuSF	3.2	1×10^{19}	film	≤ 1	[30]
BaCuSeF	2.9	1.7×10^{18}	film	1.6	[31]
BaCuTeF	2.3 (I), 3.0 (D)	1.3×10^{20}	film	8	[29], [31]
LaCuOS	3.1	1×10^{15}	film	0.2	[32]
LaCuOS	3.2	$< 1 \times 10^{19}$	film	0.5	[33]
(LaSr)CuOS	3.1	2.7×10^{20}	film	0.47	[32]
LaCuOSe	2.9	2×10^{19}	film	8	[33]
LaCuOSe:Mg	2.8	1.7×10^{21}	film	3.5	[34]
LaCuOTe	2.3	1.7×10^{17}	powder	80.6	[35]
$LaCuOSe_{0.6}Te_{0.4}$	2.6	2×10^{19}	film	0.8	[33]
BiCuOSe	1.5	1.4×10^{19}	film	4	[31]
(BiCa)CuOSe	1.5	7×10^{20}	film	2	[31]
PrCuOSe	3.1	$< 1 \times 10^{19}$	film	1.6	[33]
NdCuOS	3.1	$< 1 \times 10^{19}$	film	0.3	[33]

FIGURE CAPTIONS

Figure 1. An idealized pin double-heterojunction thin-film solar cell energy band diagram under short-circuit current conditions.

Figure 2. Energy band diagrams for a metal and a p-type semiconductor with $\Phi_M < \Phi_S$. (a) Each material is shown in isolation with all material properties referenced to the vacuum level. (b) The corresponding Schottky barrier, as defined by ideal Schottky barrier theory (i.e., charge transfer is exclusively Fermi-level-mediated, as shown by the right-going arrow in (a)).

Figure 3. Energy band diagrams for a metal and a p-type semiconductor with $\Phi_M < \Phi_S$ and $\Phi_M < \Phi_{CNL}$. (a) Each material is shown in isolation with all material properties referenced to the vacuum level. (b) The corresponding Schottky barrier, as defined by non-ideal Schottky barrier theory (i.e., ideal charge transfer is Fermi-level-mediated, as shown by the lower right-going arrow in (a), and non-ideal charge-neutrality-level-mediated, as shown by the upper right-going arrow in (a)). Non-ideal charge transfer results in the formation of a discontinuity in the local vacuum level, E_{LVAC}, with a corresponding decrease of the Schottky barrier height, ϕ_{Bp}, and the built-in potential, V_{BI}, due to the presence of a positive *microscopic* dipole, as shown in (b).

Figure 4. Energy band diagrams for a metal and a p-type semiconductor with $\Phi_M < \Phi_S$ and $\Phi_M > \Phi_{CNL}$. (a) Each material is shown in isolation with all material properties referenced to the vacuum level. (b) The corresponding Schottky barrier, as defined by non-ideal Schottky barrier theory (i.e., ideal charge transfer is Fermi-level-mediated, as shown by the lower right-going arrow in (a), and non-ideal charge-neutrality-level-mediated, as shown by the upper left-going arrow in (a)). Non-ideal charge transfer results in the formation of a discontinuity in the local vacuum level, E_{LVAC}, with a corresponding increase of the Schottky barrier height, ϕ_{Bp}, and the built-in potential, V_{BI}, due to the presence of a negative *microscopic* dipole, as shown in (b).

Figure 5. Energy band diagrams for two p-type semiconductors. (a) Each material is shown in isolation with all material properties referenced to the vacuum level. (b) The corresponding heterojunction, as defined by ideal heterojunction theory (i.e., charge transfer is exclusively Fermi-level-mediated (ideal), as shown by the left-going arrow in (a)).

Figure 6. Energy band diagrams for two p-type semiconductors with $\Phi_{CNL1} < \Phi_{CNL2}$ and $\Phi_{S1} > \Phi_{S2}$. (a) Each material is shown in isolation with all material properties referenced to the vacuum level. (b) The corresponding heterojunction, as defined by non-ideal heterojunction theory (i.e., ideal charge transfer is Fermi-level-mediated, as shown by the lower left-going arrow in (a), and non-ideal charge-neutrality-level-mediated, as shown by the upper right-going arrow in (a)). Non-ideal charge transfer results in the formation of a discontinuity in the local vacuum level, E_{LVAC}, with a corresponding increase in the conduction band discontinuity, ΔE_C, valence band discontinuity, ΔE_V, and built-in potentials, V_{BI1} and V_{BI2}, due to the presence of a positive *microscopic* dipole, as shown in (b).

Figure 7. Energy band diagrams for two p-type semiconductors with $\Phi_{CNL1} > \Phi_{CNL2}$ and $\Phi_{S1} > \Phi_{S2}$. (a) Each material is shown in isolation with all material properties referenced to the vacuum level. (b) The corresponding heterojunction, as defined by non-ideal heterojunction theory (i.e. ideal charge transfer is Fermi-level-mediated, as shown by the lower left-going arrow in (a), and non-ideal charge-neutrality-level-mediated, as shown by the upper left-going arrow in

(a)). Non-ideal charge transfer results in the formation of a discontinuity in the local vacuum level, E_{LVAC}, with a corresponding decrease in the valence band discontinuity, ΔE_V, and built-in potentials, V_{BI1} and V_{BI2}, due to the presence of a negative *microscopic* dipole, as shown in (b). Also, non-ideal charge transfer causes the conduction band discontinuity to flip from a notch to a step barrier.

Figure 8. Energy band diagrams describing the electrical interaction between molybdenum and CIGS. (a) Each material is shown in isolation with all material properties referenced to the vacuum level. Ideal Fermi-level-mediated and non-ideal charge-neutrality-level-mediated charge transfer are illustrated by the lower and upper right-going arrows, respectively. (b) The corresponding Schottky barrier between CIGS and molybdenum, as defined by ideal (solid lines) and non-ideal (dotted lines) Schottky barrier theory. The values shown in (b) for ϕ_{Bp}, V_{BI}, and W_D are obtained using non-ideal (ideal) Schottky barrier theory.

Figure 9. Energy band diagrams describing the electrical interaction between gold and CIGS. (a) Each material is shown in isolation with all material properties referenced to the vacuum level. Ideal Fermi-level-mediated and non-ideal charge-neutrality-level-mediated charge transfer are illustrated by the lower right-going arrow and upper left-going arrow, respectively. (b) The corresponding Schottky barrier between gold and CIGS, as defined by ideal (solid lines) and non-ideal (dotted lines) Schottky barrier theory. The values shown in (b) for ϕ_{Bp}, V_{BI}, and W_D are obtained using non-ideal (ideal) Schottky barrier theory.

Figure 10. Energy band diagrams describing the electrical interaction between gold and CdTe. (a) Each material is shown in isolation with all material properties referenced to the vacuum level. Ideal Fermi-level-mediated and non-ideal charge-neutrality-level-mediated charge transfer are illustrated by the lower right-going arrow and upper left-going arrow, respectively. (b) The corresponding Schottky barrier between gold and CdTe, as defined by ideal (solid lines) and non-ideal (dotted lines) Schottky barrier theory. The values shown in (b) for ϕ_{Bp}, V_{BI}, and W_D are obtained using non-ideal (ideal) Schottky barrier theory.

Figure 11. Energy band diagrams describing the electrical interaction between BCTF and aluminium. (a) Each material is shown in isolation with all material properties referenced to the vacuum level. Ideal Fermi-level-mediated charge transfer is illustrated by the lower right-going arrow. Since the metal Fermi level energy and the BCTF charge neutrality level are aligned, non-ideal charge transfer does not occur for this interface. (b) The corresponding Schottky barrier between aluminium and BCTF.

Figure 12. Energy band diagrams describing interface formation between BCTF and CIGS. (a) Each material is shown in isolation with all material properties referenced to the vacuum level. Ideal Fermi-level-mediated and non-ideal charge-neutrality-level-mediated charge transfer are illustrated by the lower left-going arrow and upper right-going arrow, respectively. (b) The corresponding heterojunction between BCTF and CIGS, as defined by ideal (solid lines) and non-ideal (dotted lines) heterojunction theory. The values shown in (b) for ΔE_C and ΔE_V are obtained using non-ideal (ideal) Schottky barrier theory.

Figure 13. Scanning electron micrograph images of the BCTF/ITO interface. (a) After a 550 $^\circ$C anneal the BCTF is clearly visible on the ITO. (b) After CIGS processing at 550 $^\circ$C, the BCTF layer is not visible. BCTF appears to have inter-diffused into the CIGS layer during the CIGS deposition process.

Figure 14. Energy band diagrams describing interface formation between Mo, $MoSe_2$, and CIGS. (a) Each material is shown in isolation with all material properties referenced to the vacuum level. Charge transfer between corresponding Fermi levels and charge neutrality levels are illustrated with arrows. (b) The corresponding heterojunction between $MoSe_2$ and CIGS, as defined by ideal (solid lines) and non-ideal (dotted lines) heterojunction theory, and the Schottky barrier between Mo and $MoSe_2$, as defined by ideal (solid lines) and non-ideal (dotted lines) Schottky barrier theory. The values shown in (b) for ΔE_C, ΔE_V, V_{BI}, and ϕ_{Bp} are obtained using non-ideal (ideal) Schottky barrier theory.

Figure 15. Energy band diagrams describing interface formation between CdTe, BCTF, and aluminium. (a) Each material is shown in isolation with all material properties referenced to the vacuum level. Charge transfer between corresponding Fermi levels and charge neutrality levels is illustrated with arrows. (b) The corresponding heterojunction between CdTe and BCTF, as defined by ideal (solid lines) and non-ideal (dotted lines) heterojunction theory, and the Schottky barrier between BCTF and aluminium, as defined by ideal (solid lines) and non-ideal (dotted lines) Schottky barrier theory. The values shown in (b) for ΔE_C, ΔE_V, and V_{BI} are obtained using non-ideal (ideal) Schottky barrier theory.

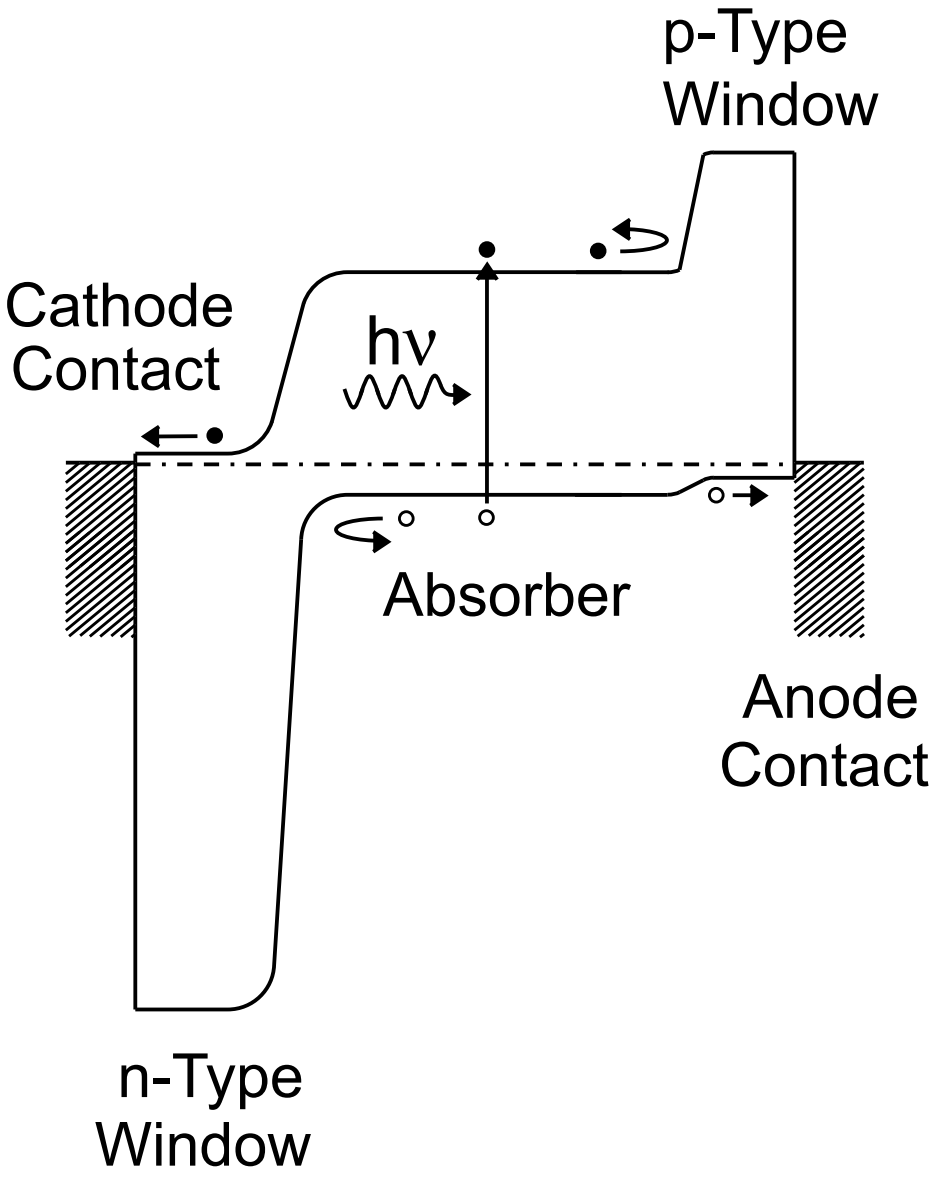

Fig. 1. Spies et al.

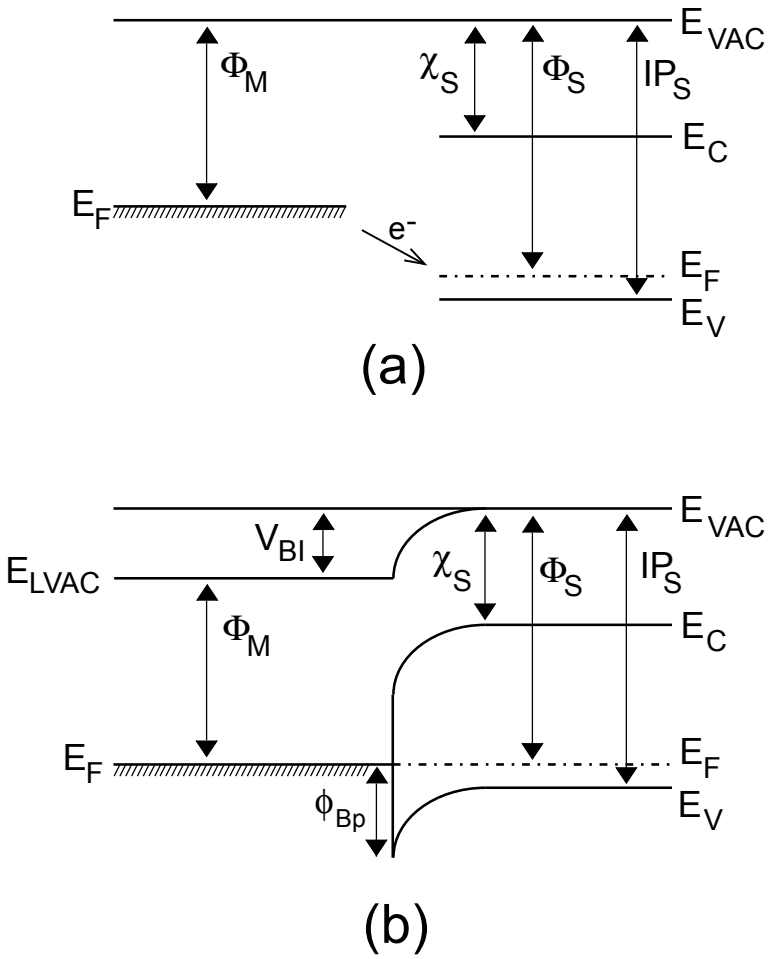

Fig. 2. Spies et al.

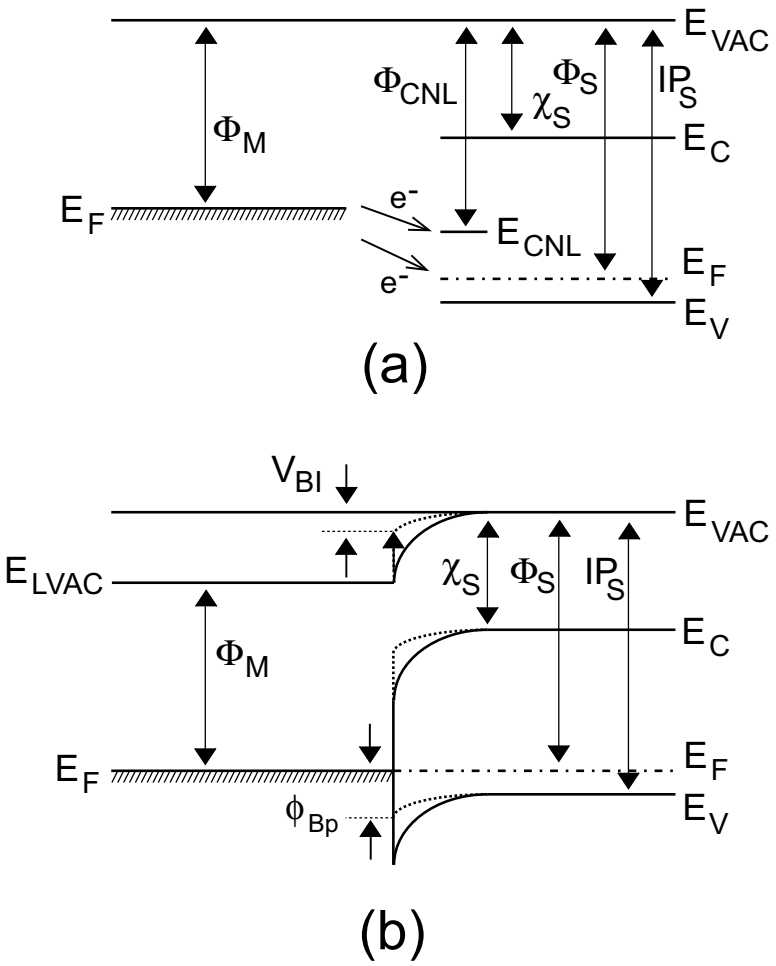

Fig. 3. Spies et al.

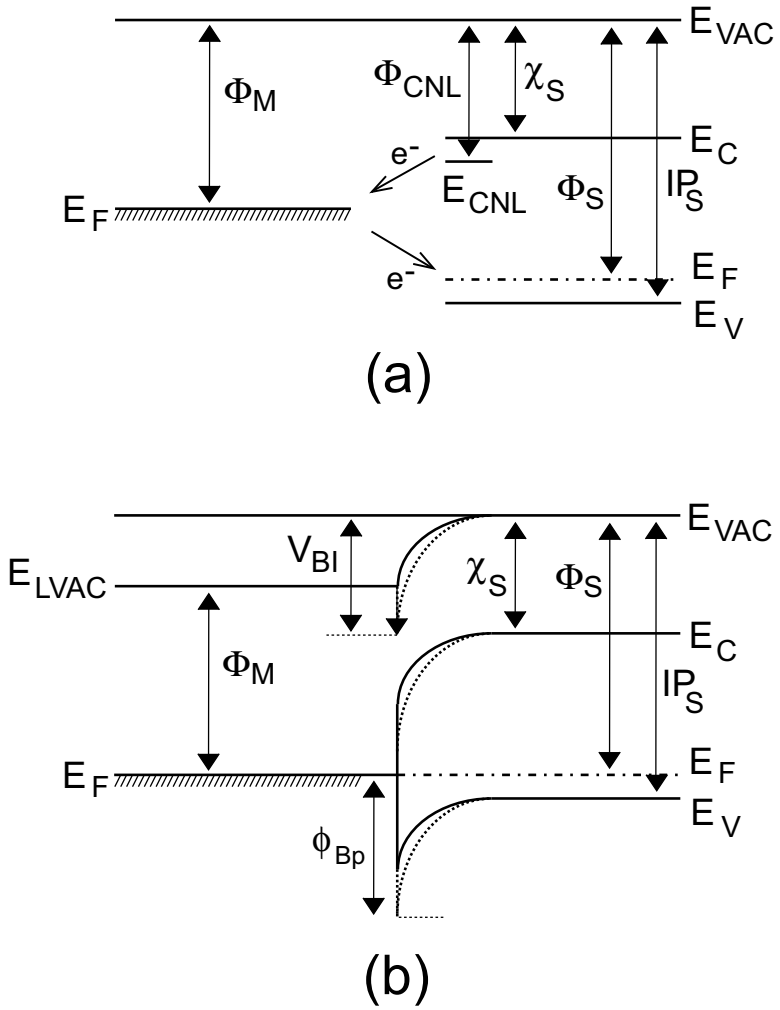

Fig. 4. Spies et al.

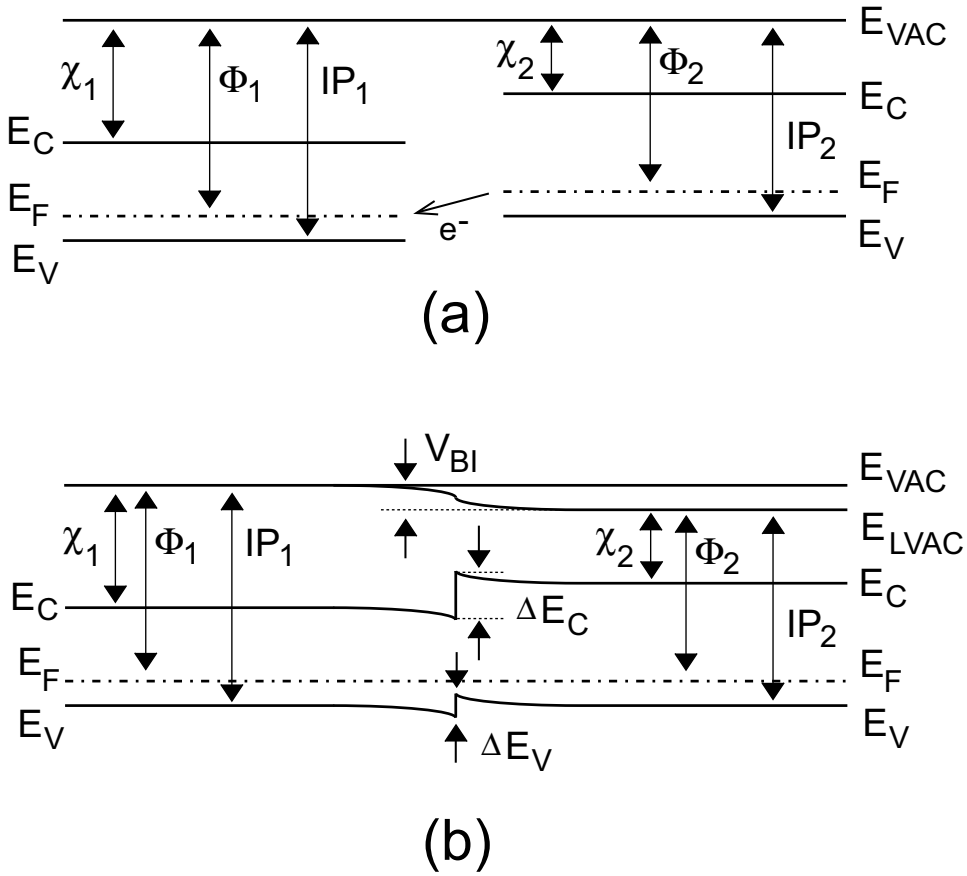

Fig. 5. Spies et al.

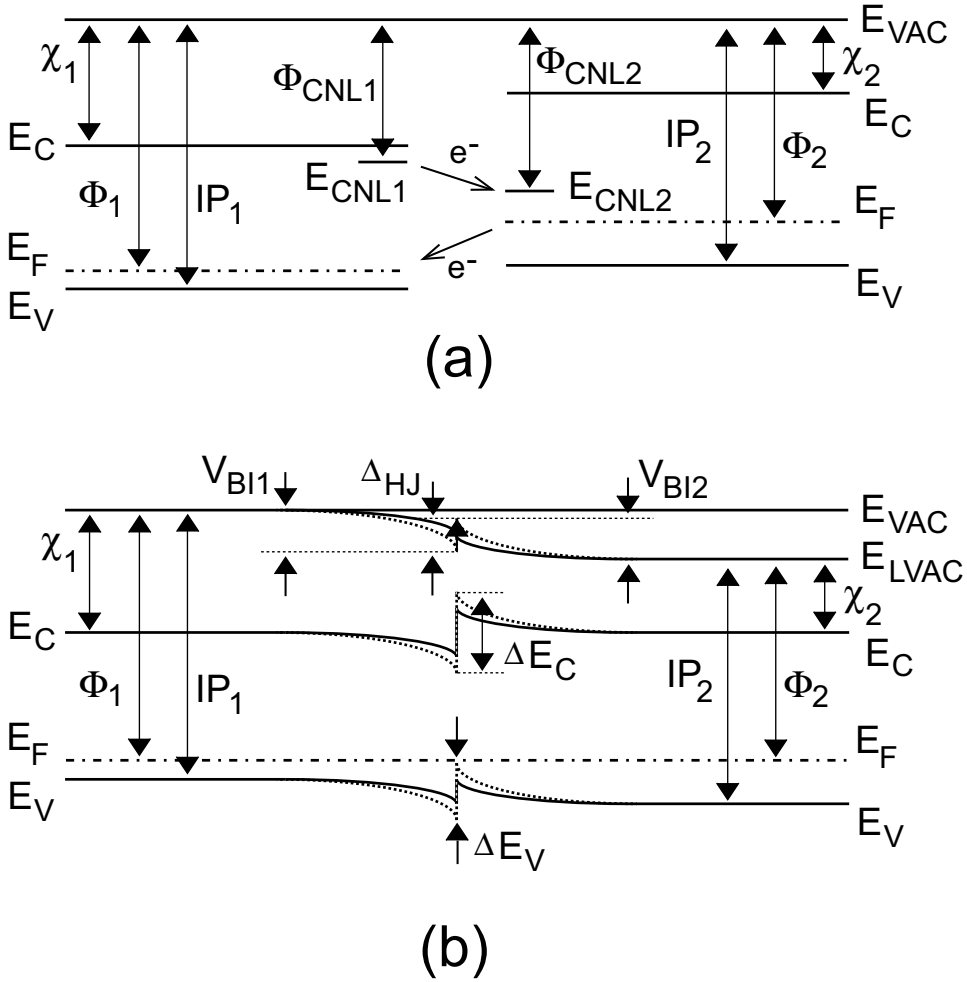

Fig. 6. Spies et al.

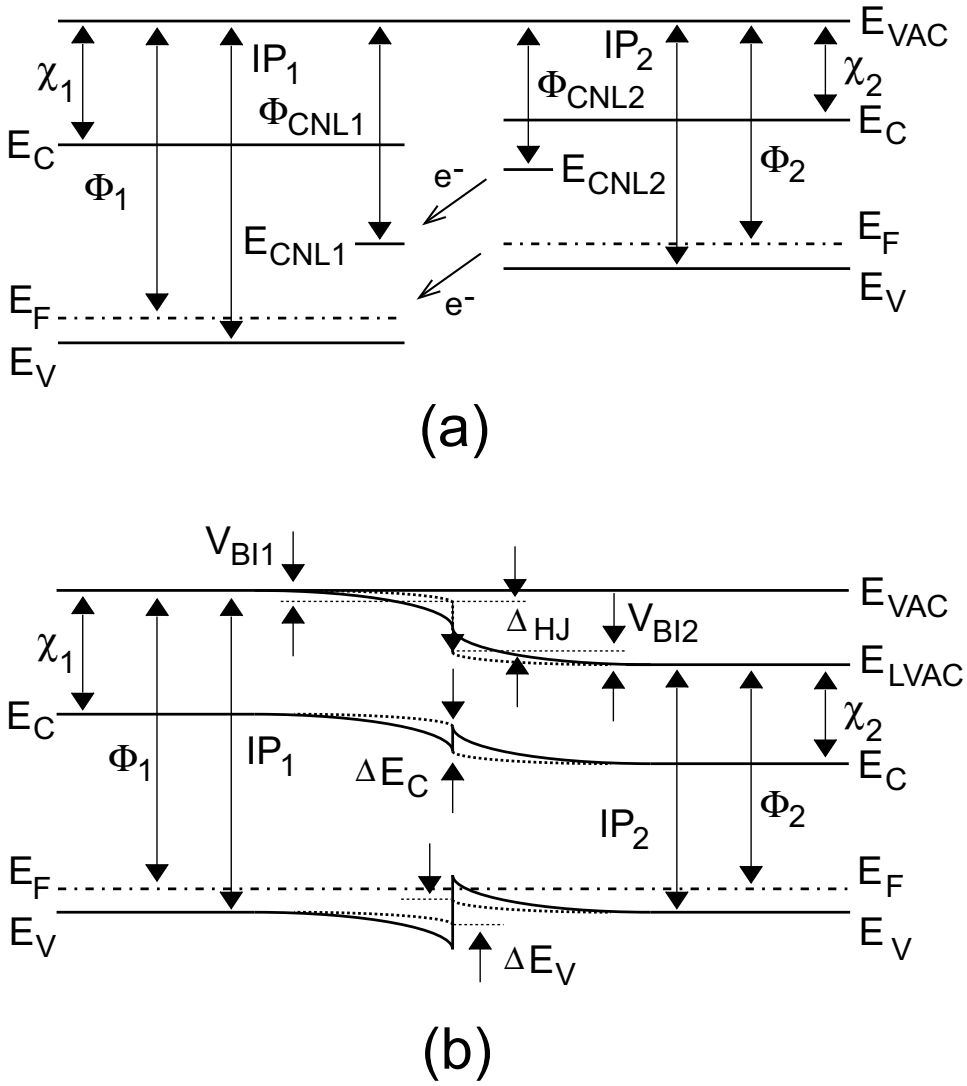

Fig. 7. Spies et al.

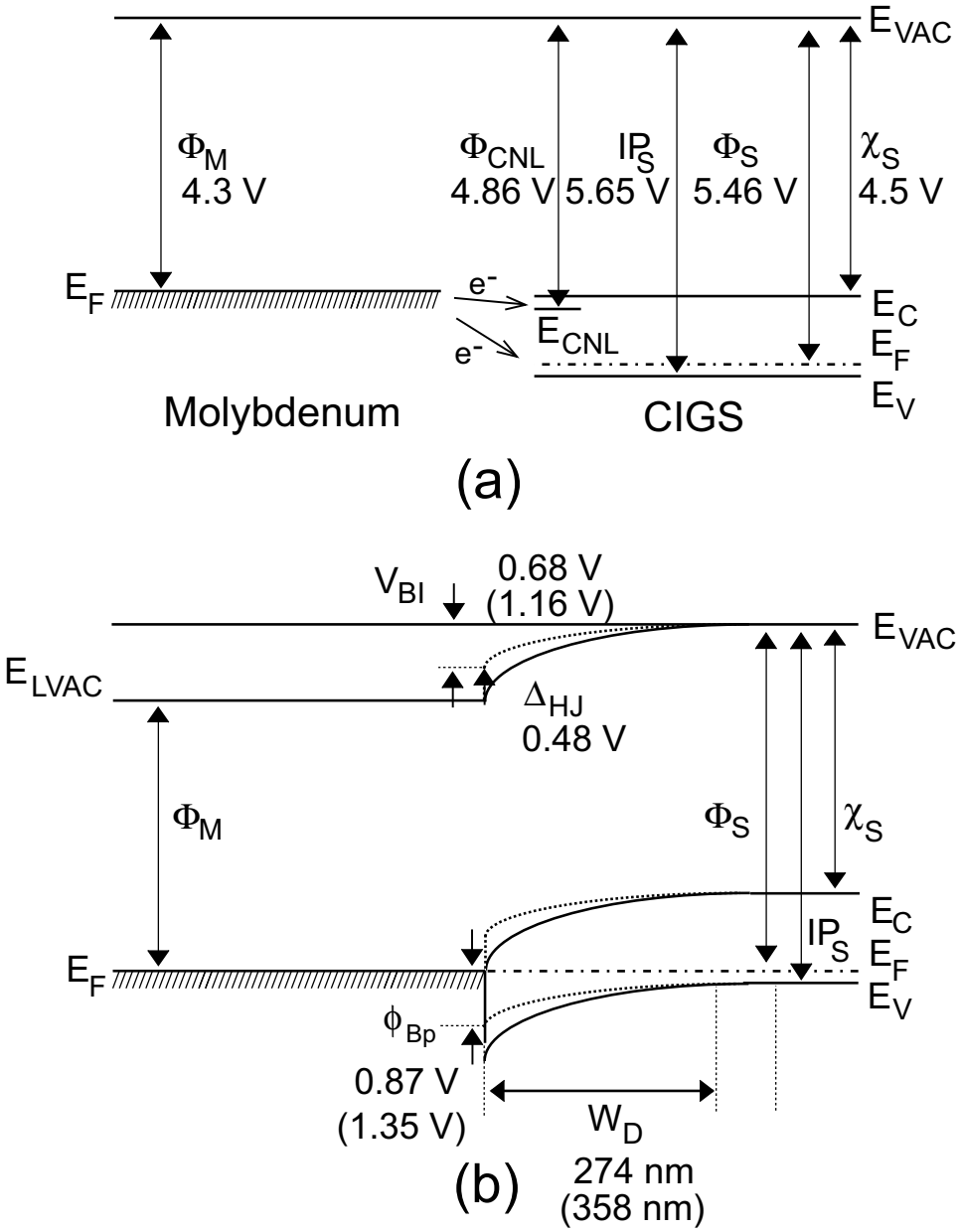

Fig. 8. Spies et al.

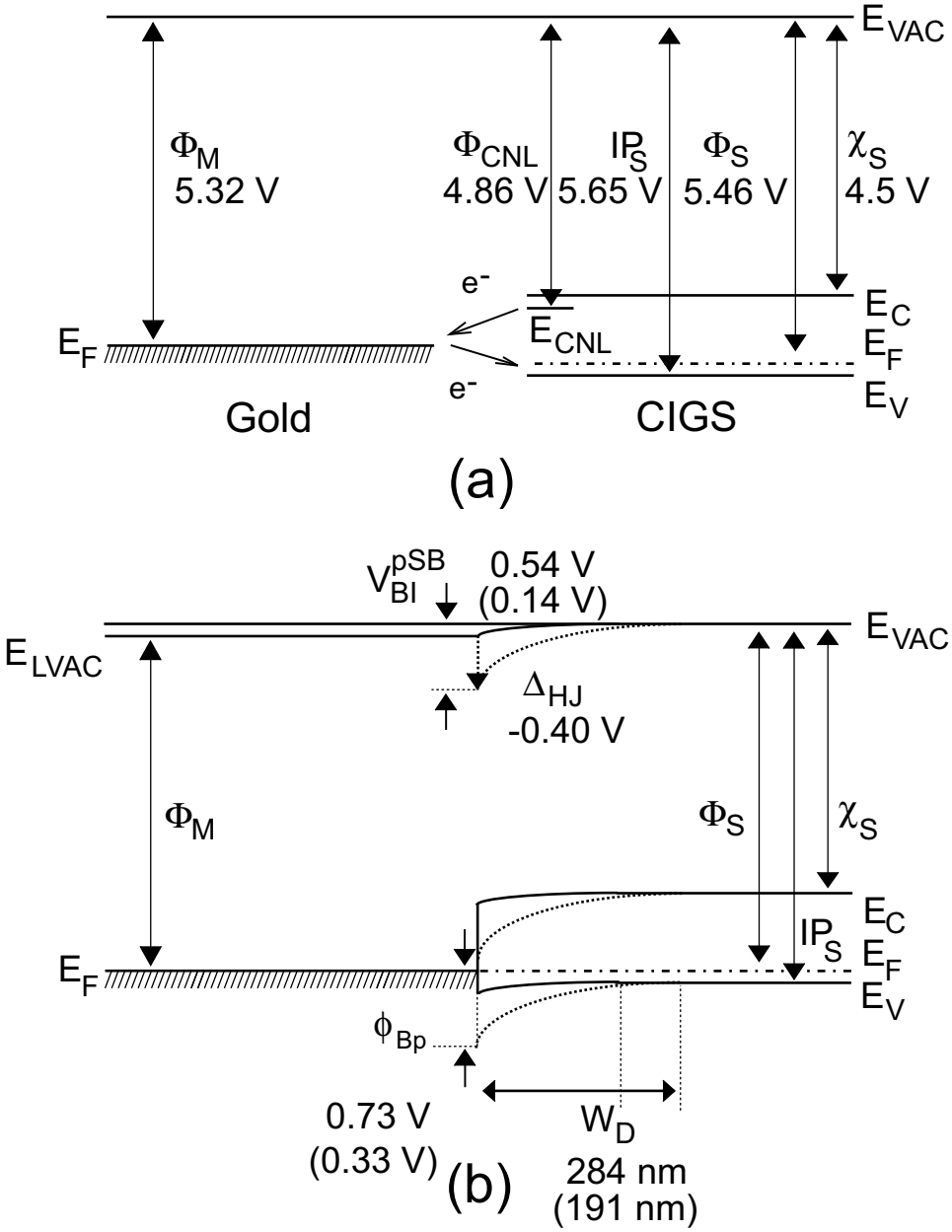

Fig. 9. Spies et al.

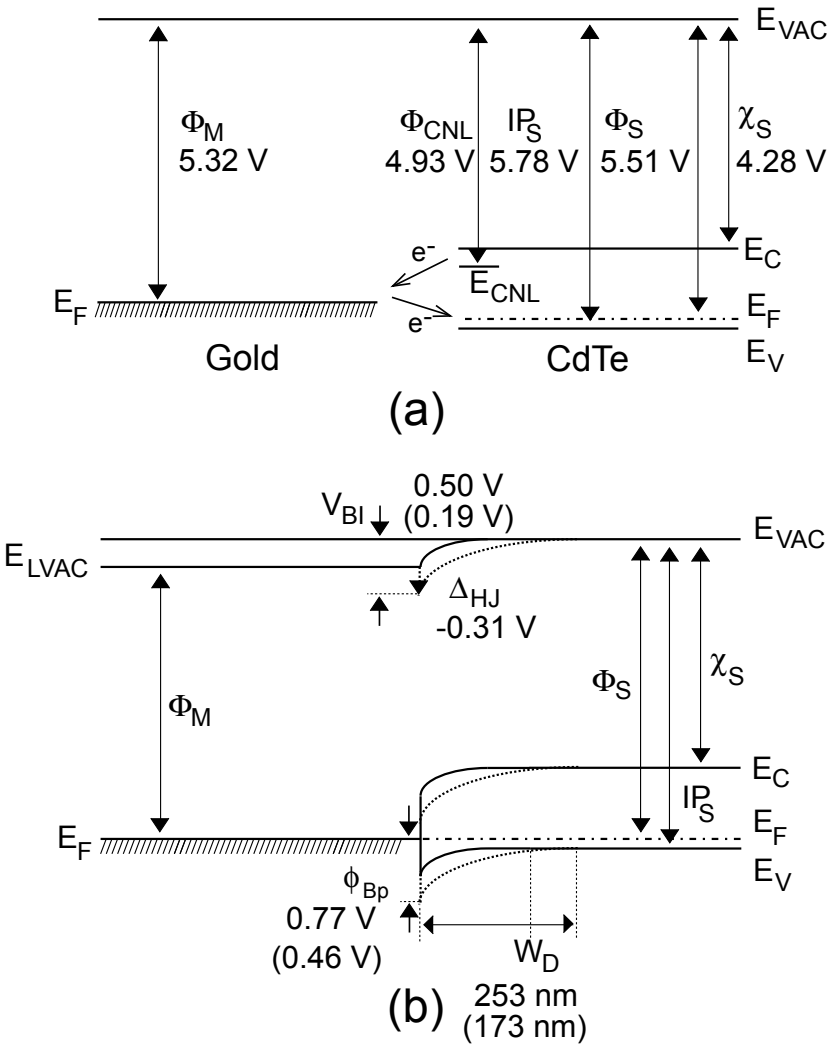

Fig. 10. Spies et al.

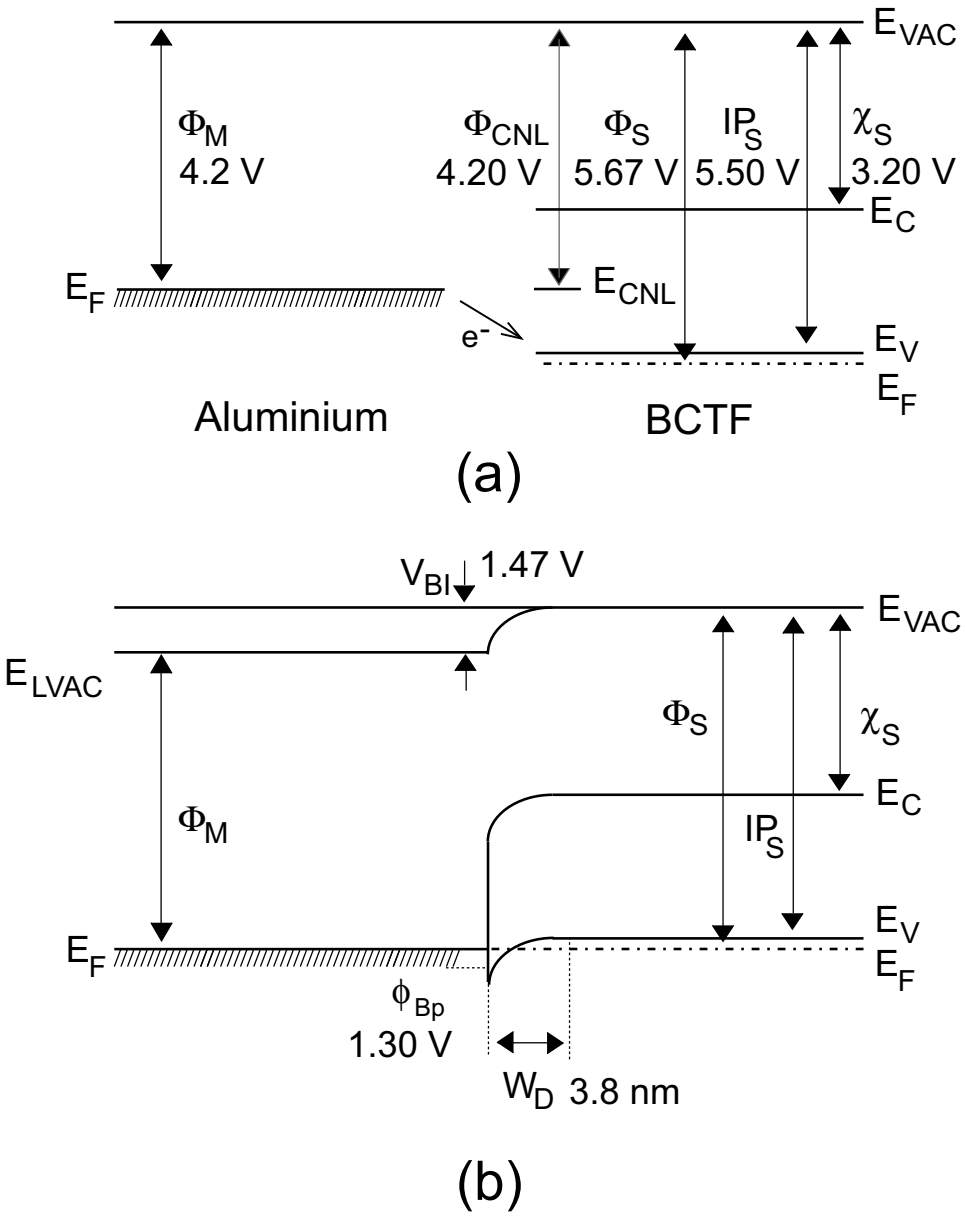

Fig. 11. Spies et al.

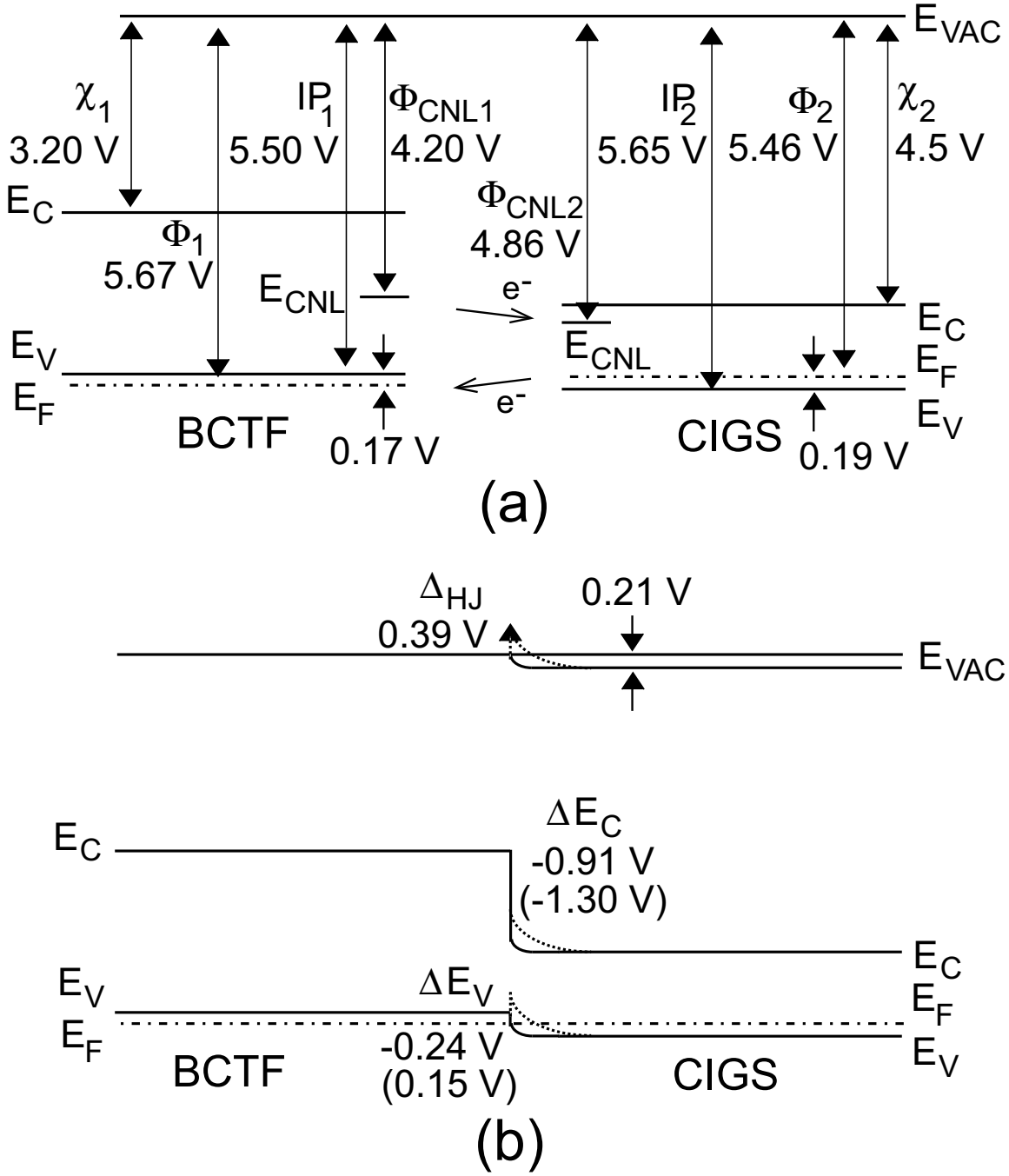

Fig. 12. Spies et al.

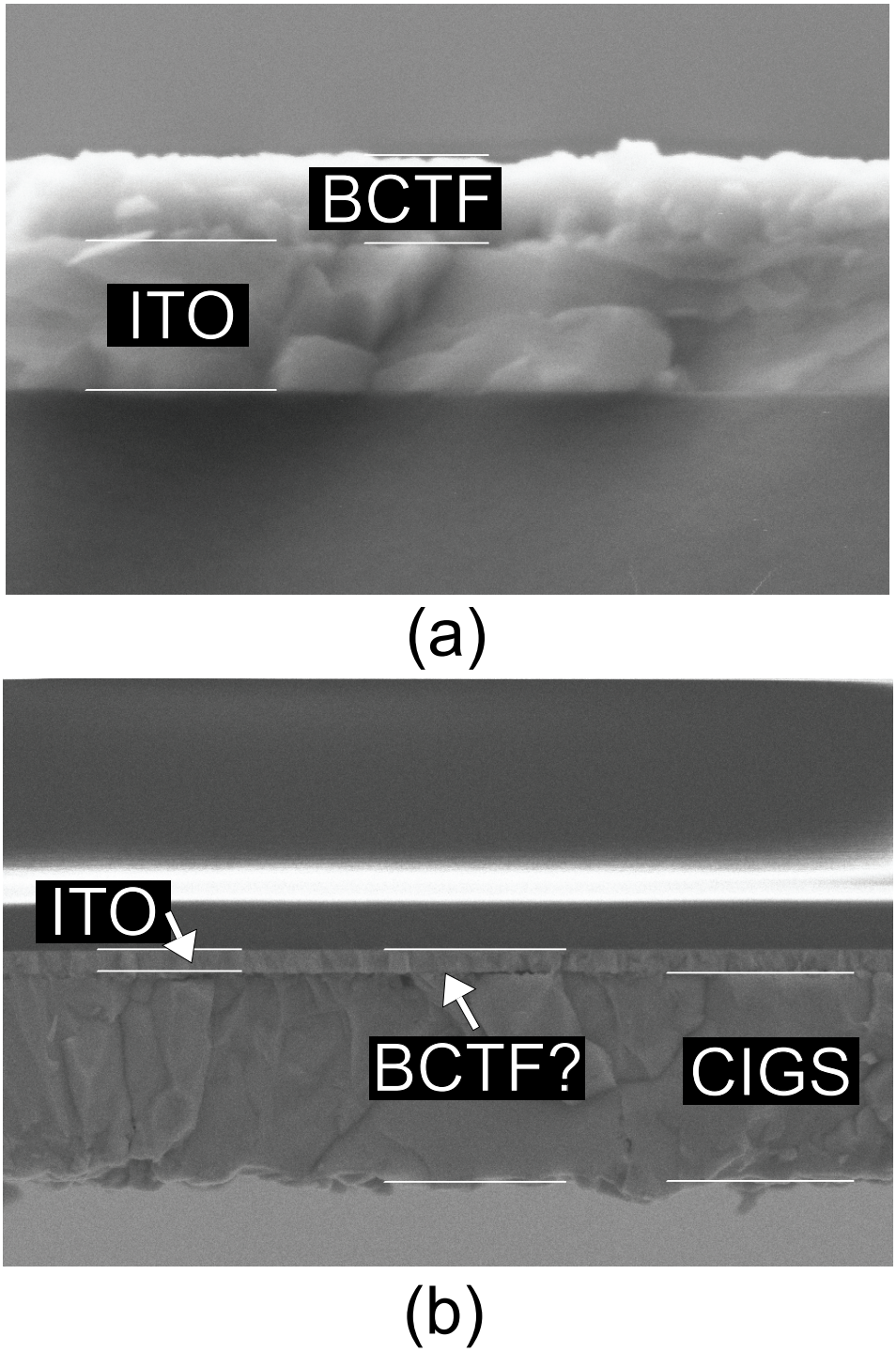

Fig. 13. Spies et al.

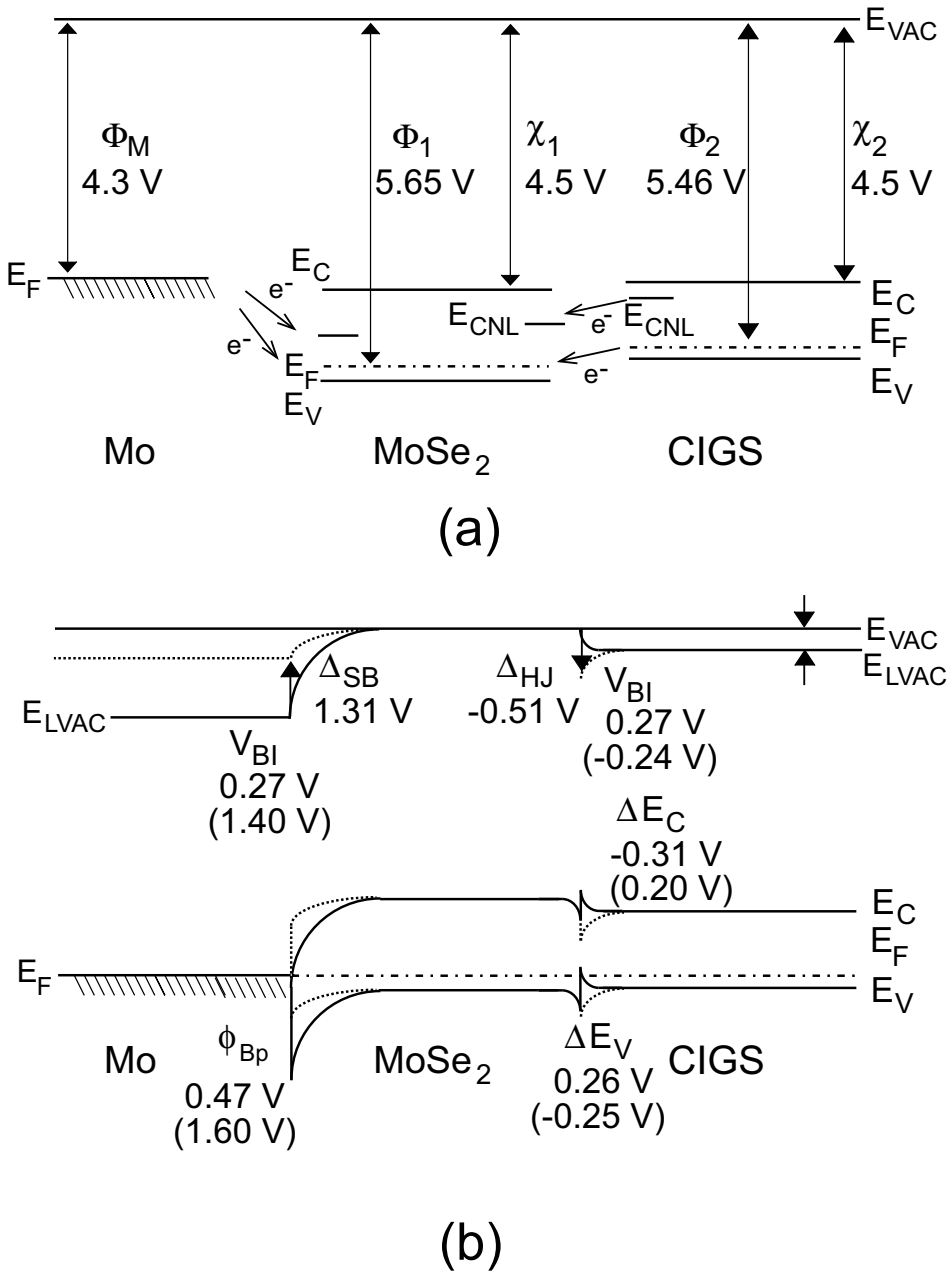

Fig. 14. Spies et al.

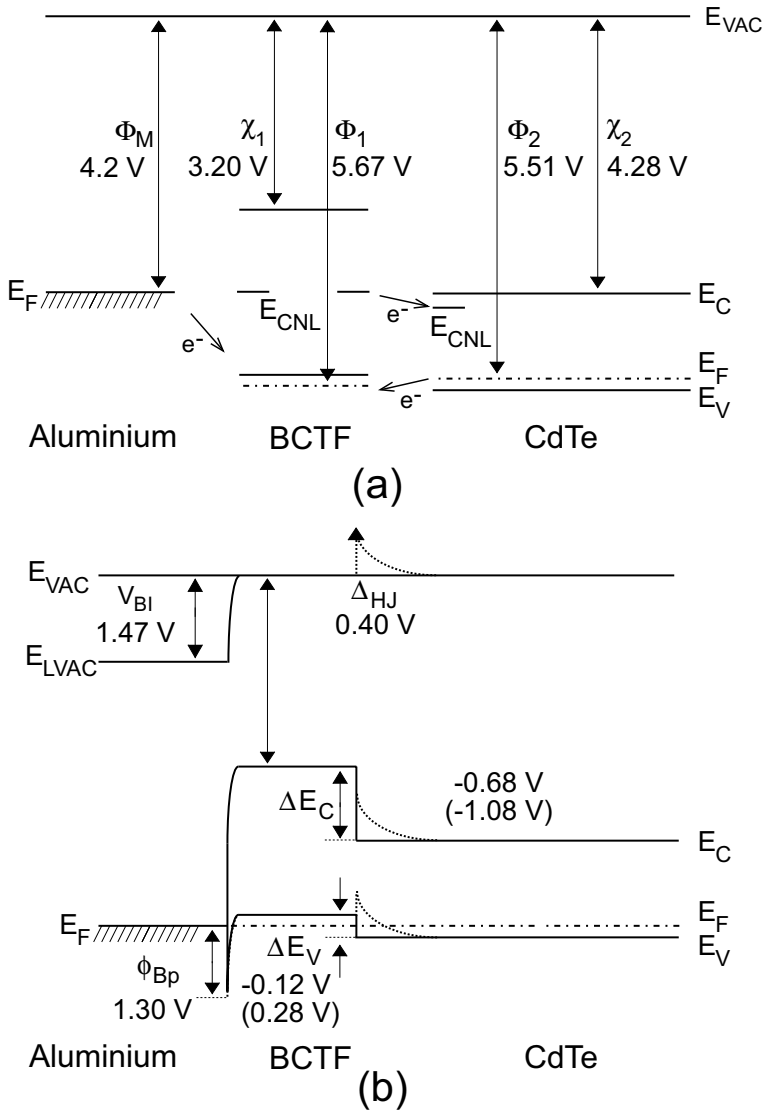

Fig. 15. Spies et al.

REPORT DOCUMENTATION PAGE

Form Approved
OMB No. 0704-0188

The public reporting burden for this collection of information is estimated to average 1 hour per response, including the time for reviewing instructions, searching existing data sources, gathering and maintaining the data needed, and completing and reviewing the collection of information. Send comments regarding this burden estimate or any other aspect of this collection of information, including suggestions for reducing the burden, to Department of Defense, Executive Services and Communications Directorate (0704-0188). Respondents should be aware that notwithstanding any other provision of law, no person shall be subject to any penalty for failing to comply with a collection of information if it does not display a currently valid OMB control number.
PLEASE DO NOT RETURN YOUR FORM TO THE ABOVE ORGANIZATION.

1. REPORT DATE *(DD-MM-YYYY)*
November 2008

2. REPORT TYPE
Subcontract Report

3. DATES COVERED *(From - To)*
26 July 2004 - 15 June 2008

4. TITLE AND SUBTITLE
Novel Materials Development for Polycrystalline Thin-Film Solar Cells: Final Subcontract Report, 26 July 2004 - 15 June 2008

5a. CONTRACT NUMBER
DE-AC36-08-GO28308

5b. GRANT NUMBER

5c. PROGRAM ELEMENT NUMBER

6. AUTHOR(S)
D.A. Keszler and J.F. Wager

5d. PROJECT NUMBER
NREL/SR-520-44020

5e. TASK NUMBER
PVA72501

5f. WORK UNIT NUMBER

7. PERFORMING ORGANIZATION NAME(S) AND ADDRESS(ES)
Oregon State University
312 Kerr Administration
Corvallis, Oregon 97331-3140

8. PERFORMING ORGANIZATION REPORT NUMBER
XAT-4-33624-11

9. SPONSORING/MONITORING AGENCY NAME(S) AND ADDRESS(ES)
National Renewable Energy Laboratory
1617 Cole Blvd.
Golden, CO 80401-3393

10. SPONSOR/MONITOR'S ACRONYM(S)
NREL

11. SPONSORING/MONITORING AGENCY REPORT NUMBER
NREL/SR-520-44020

12. DISTRIBUTION AVAILABILITY STATEMENT
National Technical Information Service
U.S. Department of Commerce
5285 Port Royal Road
Springfield, VA 22161

13. SUPPLEMENTARY NOTES
NREL Technical Monitor: Fannie Posey Eddy

14. ABSTRACT *(Maximum 200 Words)*

The simplest realization of a p-i-n double-heterojunction thin-film solar cell would consist of a lightly doped, moderate-bandgap absorber i-layer; a heavily doped, wide-bandgap n-layer window (cathode); and a heavily doped, wide-bandgap p-layer window (anode) in which the anode and cathode are electrically contacted by at least one transparent conductor. The focus herein is on p-layer interfacial assessment, which is accomplished using modern Schottky barrier and heterojunction theory and is directed to the analysis of p-windows for copper indium gallium diselenide (CIGS) and cadmium telluride (CdTe) thin-film solar cells. A p-type window layer serves as an electron reflector and also aids in the formation of an ohmic anode contact. Ohmic anode contacts are particularly difficult to form in CIGS and CdTe thin-film solar cells since these materials have very large ionization potentials and significant interfacial screening, characterized by extremely small Schottky barrier interface parameters, i.e., S = 0.14 (CIGS) and 0.21 (CdTe). An ideal p-type window material would be heavily doped, p-type, and would have a wide bandgap, a large ionization potential, and a smaller charge neutrality level energy than that of the absorber layer.

15. SUBJECT TERMS
PV; polycrystalline; solar cells; thin film; Schottky barrier; heterojunction; CIS; CdTe; window material;

16. SECURITY CLASSIFICATION OF:			17. LIMITATION OF ABSTRACT	18. NUMBER OF PAGES	19a. NAME OF RESPONSIBLE PERSON
a. REPORT	b. ABSTRACT	c. THIS PAGE			19b. TELEPHONE NUMBER (*Include area code*)
Unclassified	Unclassified	Unclassified	UL		

Standard Form 298 (Rev. 8/98)
Prescribed by ANSI Std. Z39.18

F1146-E(09/2007)